Probing Beyond the Standard Model with Supersymmetry in Vector Boson Scattering

by

Marina Stefanyk
B.Sc., Thompson Rivers University, 2021

A Thesis Submitted in Partial Fulfillment of the
Requirements for the Degree of

MASTER OF SCIENCE

in the Department of Physics and Astronomy

We acknowledge and respect the Lək̓ʷəŋən (Songhees and Xʷsepsəm / Esquimalt) Peoples on whose territory the university stands, and the Lək̓ʷəŋən and W̱SÁNEĆ Peoples whose historical relationships with the land continue to this day.

Probing Beyond the Standard Model with Supersymmetry in Vector Boson Scattering

by

Marina Stefanyk
B.Sc., Thompson Rivers University, 2021

Supervisory Committee

Dr. D. Morrissey, Co-supervisor
(Department of Physics and Astronomy)

Dr. H. Russell, Co-supervisor
(Department of Physics and Astronomy)

Dr. M. Lefebvre, Departmental Member
(Department of Physics and Astronomy)

Abstract

The purpose of this thesis is to analyze the potential for measurements of Standard Model vector boson scattering to probe new physics lighter than the TeV scale. Supersymmetry (SUSY) is one example of a beyond the Standard Model theory that contains a dark matter candidate. The Minimal Supersymmetric Standard Model (MSSM) provides a well-developed framework to construct illustrative test cases. Various Bino-Wino models, simplified versions of the MSSM, are utilized to cover a range of chargino and neutralino masses. The lightest superpartner, a neutralino, is the dark matter candidate. Simulations are used to explore the potential impact of SUSY signals on the phase spaces used by ATLAS and CMS to measure opposite sign W boson scattering. Upper limits on the SUSY signals are obtained by comparing the SUSY predictions to results from experimental vector boson scattering measurements performed at the LHC by ATLAS and CMS. The limits are weaker than those obtained with direct SUSY searches by ATLAS and CMS. Thus, light new physics of this subset of SUSY will not contaminate Standard Model opposite sign W boson scattering measurements.

Table of Contents

List of Tables

List of Figures

Acknowledgements

I would like to thank:

My supervisors, for their endless support, patience, and understanding.

Pacific Animal Therapy Society, for introducing me to Brodie, Morley, Jura, Big Sadie, Little Sadie, Moose, and Forrest.

My parents, for making sure I always had something to look forward to.

I hold a cup of wisdom
Kate Bush

Dedication

To Bruce and Bella

Chapter 1

Introduction

The Standard Model (SM) of particle physics describes the fundamental particles and their interactions. It is an exceptionally predictive model with many predictions subsequently confirmed by observations, including recently using data collected by the ATLAS and CMS detectors at the Large Hadron Collider (LHC). However, there are also observations that cannot be accounted for by the SM alone including, but not limited to, the existence of dark matter, that have lead to searches for Beyond the Standard Model (BSM) physics and ways to extend the SM. As more data is collected at the LHC, rarer processes with smaller production rates can start to be accurately measured. One such process recently measured is electroweak production of opposite sign W bosons in association with two jets (EWK W^+W^-jj). Contained in this signal are interactions referred to as vector boson scattering (VBS). VBS is exceptionally sensitive to BSM physics. New, cutting edge measurements being done in phase spaces not previously accessible, such as EWK W^+W^-jj, may observe BSM effects.

The goal of this project is to explore the potential sensitivity of vector boson scattering measurements to BSM physics. Supersymmetry (SUSY) is an extension to the SM that predicts BSM particles that could mimic SM particle signals in current detectors. Specifically, SUSY is one model of BSM physics that could affect VBS measurements by contaminating the phase space.

In this thesis, BSM particle production is simulated and compared to experimental SM measurements of EWK W^+W^-jj to assess the potential impact of new, light BSM particles. A profile likelihood test is used to set limits on the BSM signal cross-sections. Rare processes with large backgrounds such as VBS are difficult measurements that have large uncertainties. Though the current measurements are largely in agreement with the SM, BSM effects may also be contained within the uncertainty band. Increased precision in future measurements could resolve those effects. If there is a possible signal to untangle, it is a motivator to analyze

areas with difficult backgrounds. This thesis investigates potential existence of SUSY within W^+W^- VBS measurements.

This thesis is organized as follows:

- **Chapter 2** provides a review of the Standard Model of particle physics, and describes the process of vector boson scattering.
- **Chapter 3** reviews evidence and motivation for physics beyond the Standard Model. The Bino-Wino supersymmetric model is introduced along with its current bounds.
- **Chapter 4** outlines the steps to simulate processes with Monte Carlo event generation. A short description of particle detectors is included.
- **Chapter 5** describes the simulation of the Bino-Wino model and the systematic uncertainties.
- **Chapter 6** details the statistical tests used to set upper limits including the profile likelihood function and the CL_s procedure using toys.
- **Chapter 7** presents the results.
- **Chapter 8** concludes the thesis, and provides a look at future work.

Chapter 2

Standard Model

The Standard Model (SM) is a theory that describes the known elementary particles that make up matter and mediate interactions [1, 2, 3]. Fermions are particles with $\frac{1}{2}$-spin; they obey Fermi-Dirac statistics [3]. There are twelve types of fermions in the SM: six quarks and six leptons. The quarks are up (u), down (d), charm (c), strange (s), top (t), and bottom (b) [2]. Quarks participate in strong interactions and transform under the $SU(3)$ gauge group; the property that transforms is called colour [1]. Quarks are assigned a colour charge of red, blue, green, antired, antiblue, or antigreen [1]. The leptons are electron (e), muon (μ), tau (τ), and a corresponding neutrino for each (ν_e, ν_μ, ν_τ) [2]. Leptons are not charged under strong interactions and therefore do not have colour[2]. Anti-particles are the charge conjugates of the particles and are denoted with a bar, e.g. $\overline{q}$ [2].

Bosons have integer spin and obey Bose-Einstein statistics [3]. Gauge bosons, also called vector bosons, are force carriers that mediate interactions [3]. Massive vector bosons can be characterized by their mass and spin. The charged $W^{\pm}$ and the neutral Z bosons are massive, have spin-1, and mediate the weak interactions [1]. They have three physical polarizations; two transverse and one longitudinal [3]. Massless vectors bosons can be characterized by their helicity. They have two physical, transverse polarizations [4]. The photon (γ) is massless and mediates the electromagnetic interactions [1]. There are eight massless gluons (g) that mediate the strong interactions [5].

The Higgs boson is spin-0 and plays a role in giving mass to the other fundamental particles [3]. It is the only fundamental scalar boson in the SM [5].

2.1 Structure of the Standard Model

The Standard Model is based on a non-abelian $SU(3)_C \times SU(2)_L \times U(1)_Y$ gauge group [1, 2]. The $U(1)$ symmetry is associated with a charge, Y, called hypercharge [3, 5]. The

Fermion	Quantum Number $(SU(3)_C,\ SU(2)_L,\ U(1)_Y)$
$Q_L = \begin{pmatrix} u_L \\ d_L \end{pmatrix}$	$(\mathbf{3}, \mathbf{2}, \frac{1}{6})$
u_R	$(\mathbf{3}, \mathbf{1}, \frac{2}{3})$
d_R	$(\mathbf{3}, \mathbf{1}, -\frac{1}{3})$
$L_L = \begin{pmatrix} \nu_L \\ e_L \end{pmatrix}$	$(\mathbf{1}, \mathbf{2}, -\frac{1}{2})$
e_R	$(\mathbf{1}, \mathbf{1}, -1)$
Complex Scalar Field	
$H = \begin{pmatrix} H^+ \\ H^0 \end{pmatrix}$	$(\mathbf{1}, \mathbf{2}, \frac{1}{2})$

Table 2.1: Representations of SM fermion fields and Higgs field and their quantum numbers for the associated gauge groups [2].

$SU(3)_C$ symmetry corresponds to the strong force [1]. The $SU(2)_L \times U(1)_Y$ symmetry is spontaneously broken and dictates the electroweak force, a combination of both the weak force and electromagnetic forces [2]. Gravity is not included in the Standard Model [5].

The fermions are organized into three generations; each generation has the same properties but different masses [2]. The generations are labeled with a flavour index. Fermions, represented as Weyl spinors, have a property called chirality, which is also referred to as handedness [3]. They can be left- or right-handed and this is denoted with an L or R subscript [3].

The quantum numbers of a representation of a SM field indicate how they transform when acted on by the different gauge groups [5]. The quantum number value **1** indicates the trivial representation. A quantum number N under $SU(N)$ indicates the dimension of the representation and a transformation in the fundamental representation. For example, quarks have quantum number three under $SU(3)$ which means they transform in the fundamental, three-dimensional representation of $SU(3)$, and the property that transforms is colour [2]. Conversely, leptons have quantum number one under $SU(3)$; they do not transform under $SU(3)$ and do not possess colour [2]. The quantum numbers of the SM fermions and Higgs field are listed in Table 2.1. The left-handed quarks and leptons are represented as doublets while the right-handed fermions are singlets; only the left-handed fermions transform under $SU(2)$. The quantum numbers of the gauge fields are listed in Table 2.2.

The SM Lagrangian is of the form

Gauge Field	Quantum Number $(SU(3)_C,\ SU(2)_L,\ U(1)_Y)$
G^a_μ	$(\mathbf{8},\mathbf{1},0)$
W^p_μ	$(\mathbf{1},\mathbf{3},0)$
B_μ	$(\mathbf{1},\mathbf{1},0)$

Table 2.2: Representations of the gauge fields and their associated quantum numbers [2].

$$\mathcal{L}_{\text{SM}} = \mathcal{L}_{\text{gauge}} + \mathcal{L}_{\text{Higgs}} + \mathcal{L}_{\text{Yukawa}} \ , \tag{2.1}$$

where $\mathcal{L}_{\text{gauge}}$ contains the kinetic terms [1]. The field strength tensor $F^a_{\mu\nu}$ is defined as

$$F^a_{\mu\nu} = \partial^a_\mu A_\nu - \partial^a_\nu A_\nu - g f^{abc} A^b_\mu A^c_\nu \ , \tag{2.2}$$

where f^{abc} is the structure constant defined by the generators t_i of a group and the Lie algebra $[t_a, t_b] = i f^{abc} t_c$ [5]. If the field is abelian, the third term in Eq. (2.2) is zero. The gauge field strength of $SU(3)$ is called the gluon field strength $G_{\mu\nu}$. The $SU(2)$ gauge field strength is

$$W^a_{\mu\nu} = \partial_\mu W^a_\nu - \partial_\nu W^a_\mu - i g \epsilon_{abc} W^b_\mu W^c_\nu \ , \tag{2.3}$$

and the $U(1)$ hypercharge field strength is $B_{\mu\nu} = \partial_\mu B_\nu - \partial_\nu B_\mu$ [2]. The field $G_{\mu\nu}$ couples to fermions with colour, $W_{\mu\nu}$ couples to left-handed fermions, and $B_{\mu\nu}$ couples to fermions with hypercharge. The gauge field kinetic terms are [1, 2]

$$\begin{aligned}\mathcal{L}_{\text{gauge}} = -\frac{1}{4} B_{\mu\nu} B^{\mu\nu} - \frac{1}{4} W^p_{\mu\nu} W^{p\ \mu\nu} - \frac{1}{4} G^a_{\mu\nu} G^{a\ \mu\nu} \\ + \overline{Q}_L i\gamma^\mu \mathcal{D}_\mu Q_L + \overline{u}_R i\gamma^\mu \mathcal{D}_\mu u_R + \bar{d}_R i\gamma^\mu \mathcal{D}_\mu d_R \\ + \overline{L}_L i\gamma^\mu \mathcal{D}_\mu L_L + \bar{e}_R i\gamma^\mu \mathcal{D}_\mu e_R .\end{aligned} \tag{2.4}$$

The covariant derivative $\mathcal{D}_\mu$ has the form

$$\mathcal{D}_\mu = \partial_\mu - i g_s t^a_c G^a_\mu - i g\, t^p_L W^p_\mu - i g' Y B_\mu, \tag{2.5}$$

where g_S, g, and g' are the coupling constants for $SU(3)$, $SU(2)$, and $U(1)$, respectively [1]. The generators for $SU(2)$ are $t^p_L = \frac{1}{2}\sigma^p$, where σ^p are the Pauli matrices [1]. The Higgs term

is [3]

$$\mathcal{L}_{\text{Higgs}} = \left| \left(\partial_\mu + ig\frac{\sigma^p}{2} W_\mu^p + ig'\frac{1}{2} B_\mu \right) H \right|^2 - \left(-\mu^2 |H|^2 + \frac{\lambda}{2} |H|^4 \right) . \tag{2.6}$$

The first bracketed term in Eq. 2.6 contains kinetic terms and the second bracketed term is the Higgs potential [3]. The Yukawa terms connect the fermions to the scalar Higgs field,

$$\mathcal{L}_{\text{Yukawa}} = -y_d \bar{Q} H d_R - y_u \bar{Q} \tilde{H} u_R - y_e \bar{L} H e_R + \text{h.c.}, \tag{2.7}$$

where y_d, y_u, y_e are the Yukawa coupling constants for down-type quarks, up-type quarks, and left-handed leptons, respectively and $\tilde{H} \equiv i\sigma_2 H^\star$ [3].

2.2 Electroweak Symmetry Breaking

Spontaneous symmetry breaking (SSB) leads to vector boson masses through the Higgs mechanism [3, 5]. While the breaking directly leads to the electroweak gauge bosons acquiring masses, the fermions require Yukawa couplings to acquire mass [3, 5]. The broken $SU(2) \times U(1)_Y$ symmetry gives rise to three Goldstone bosons, corresponding to the generators of the broken symmetry [1]. The $SU(2)$ Higgs doublet can be written in the unitary gauge,

$$H(x) = \frac{1}{\sqrt{2}} \begin{pmatrix} 0 \\ v + h(x) \end{pmatrix} , \tag{2.8}$$

with a vacuum expectation value $v = \sqrt{\mu^2/\lambda}$; $h(x)$ is the real scalar field Higgs boson [3, 5]. When inserted into the kinetic Higgs term in Eq. (2.6), mass is acquired for the gauge bosons associated with the broken symmetry, W_μ^p and B^μ, and the Goldstone bosons do not appear [3]. The gauge bosons absorb the degrees of freedom from the Goldstone bosons and gain longitudinal polarizations [3].

The Yukawa interactions, represented in Eq. (2.7), generate masses for the fermions after electroweak symmetry breaking [3]. The Yukawa terms post breaking show that the masses of the fermions are proportional to how strong they couple to the Higgs field [5]. The doublet $H(x)$ does not transform under $SU(3)$, so $SU(3)$ remains unbroken. Within the broken $SU(2)_L \times U(1)_Y$ there is a maximal unbroken subgroup, $U(1)$, generated by $Q \equiv t_L^3 + Y$, which is identified as $U(1)_{EM}$ [3]. The generator of $U(1)_{EM}$, Q, corresponds to electric charge and is associated with the photon, a massless vector boson [3]. The gauge boson mass matrix

comes from the covariant kinetic term:

$$|D_\mu H|^2 \to \frac{1}{2}\partial + \frac{1}{2}\frac{v^2}{2}\left[g^2[(W_\mu^1)^2 + (W_\mu^2)^2] + (-gW_\mu^3 + g'B_\mu)^2\right] + ... \tag{2.9}$$

where the ellipse represents higher order terms and terms without electroweak fields [1]. The two charged gauge W bosons combine to make the $W^\pm$ bosons of the weak interaction [5]:

$$W_\mu^\pm = \frac{1}{\sqrt{2}}(W_\mu^1 \mp iW_\mu^2) \ , \tag{2.10}$$

which have measured mass [5, 6]

$$M_W = \frac{gv}{2} = 80.3692 \pm 0.0133\,\text{GeV} \ . \tag{2.11}$$

The Z boson and the photon, γ, are related to the neutral gauge bosons W^0 and B through the weak mixing angle θ_W [5]

$$\cos\theta_W = c_W = \frac{g}{\sqrt{g^2+g'^2}} \ , \quad \sin\theta_W = s_W = \frac{g'}{\sqrt{g^2+g'^2}} \ , \tag{2.12}$$

and the transformation

$$\begin{pmatrix} Z_\mu \\ A_\mu \end{pmatrix} = \begin{pmatrix} c_W & -s_W \\ s_W & c_W \end{pmatrix} \begin{pmatrix} W_\mu^3 \\ B_\mu \end{pmatrix} . \tag{2.13}$$

The field A_μ has a zero eigenvalue and corresponds to the massless photon γ. The Z boson has measured mass [6]

$$M_Z = \frac{v}{2}\sqrt{g^2+g'^2} = 91.1880 \pm 0.0020\,\text{GeV}. \tag{2.14}$$

Gauge covariant derivatives dictate SM vector boson interactions with the fermions.

The Higgs boson is the excitation around the minimum of the Higgs potential, and has mass [1, 6]

$$M_h = \sqrt{2\lambda v^2} = \sqrt{2\mu^2} = 125.20 \pm 0.11\,\text{GeV} \ . \tag{2.15}$$

The electroweak sector of the SM contains the parameters g, g', and v which cannot be calculated from first principals but are fixed by measurements of the W and Z boson masses, and the fine structure constant (α). The Higgs boson mass measurement fixes λ and μ^2 via Eq. (2.15).

In the Standard Model, quark number, baryon number, and lepton number are con-

Boson	Mass [GeV]	Electric Charge
$W^{\pm}$	80.3692 ± 0.0133	$\pm$
Z^0	91.1880 ± 0.0020	0
H^0	125.20 ± 0.11	0
γ	0	0

Table 2.3: The current measured masses of the electroweak gauge bosons from the PDG [6].

served [7]. All terms conserve charge conjugation (C), parity (P), and time reversal (T) except in terms where W or Z bosons couple to fermions. Fermion number is conserved except for couplings to W boson [7]. The W and Z couplings violate P and C but conserve joint CP symmetry [7].

2.3 Vector Boson Scattering

The SM gauge group $SU(2)$ is non-abelian; the commutator in Eq. (2.3) is non zero and results in a quadratic term [1]. Due to the quadratic term in Eq. (2.3), the kinetic term in Eq. (2.4) gives rise to cubic and quartic terms [3, 8]. These terms represent self-interactions of the gauge fields. The corresponding Feynman diagram vertices are shown in Figure 2.1. The cubic terms are [8]

$$\begin{aligned}\mathcal{L}_3 = &-ie\cot\theta_W\{(\partial^\mu W^\nu - \partial^\nu W^\mu)W^\dagger_\mu Z_\nu - (\partial^\mu W^{\nu\dagger} - \partial^\nu W^{\mu\dagger})W_\mu Z_\nu + W_\mu W^\dagger_\nu(\partial^\mu Z^\nu - \partial^\nu Z^\mu)\} \\ &- ie\{(\partial^\mu W^\nu - \partial^\nu W^\mu)W^\dagger_\mu A_\nu - (\partial^\mu W^{\nu\dagger} - \partial^\nu W^{\mu\dagger})W_\mu A_\nu + W_\mu W^\dagger_\nu(\partial^\mu A^\nu - \partial^\nu A^\mu)\} \quad (2.16)\end{aligned}$$

and the quadratic terms are [8]

$$\begin{aligned}\mathcal{L}_4 = -\frac{e^2}{2\sin^2\theta_W}&\{(W^\dagger_\mu W_\nu)^2 - W^\dagger_\mu W^{\mu\dagger} W_\nu W^\nu\} \\ &- e^2\cot^2\theta_W\{W^\dagger_\mu W^\mu Z_\nu Z^\nu - W^\dagger_\mu Z^\mu W_\nu Z^\nu\} \\ &- e^2\cot\theta_W\{2W^\dagger_\mu W^\mu Z_\nu A^\nu - W^\dagger_\mu Z^\mu W_\nu A^\nu - W^\dagger_\mu A^\mu W_\nu Z^\nu\} \\ &- e^2\{W^\dagger_\mu W^\mu A_\nu A^\nu - W^\dagger_\mu A^\mu W_\nu A^\nu\}\ . \quad (2.17)\end{aligned}$$

There are cubic interaction terms involving the Higgs boson as well [3]:

$$\mathcal{L}_h \quad = \quad 2\frac{h}{v}\left(m_W^2 W^\dagger_\mu W^\mu \ + \ \frac{1}{2}m_Z^2 Z^2_\mu\right) \ + \ \left(\frac{h}{v}\right)^2\left(m_W^2 W^\dagger_\mu W^\mu \ + \ \frac{1}{2}m_Z^2 Z_\mu Z_\mu\right) \quad . \quad (2.18)$$

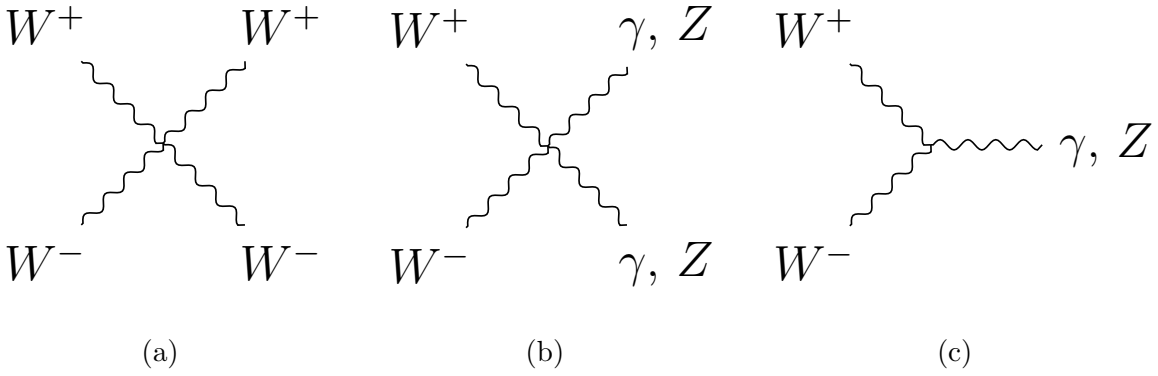

(a) (b) (c)

Figure 2.1: The SM gauge boson self-interaction vertices. Figure 2.1a shows the quartic $WWWW$ coupling. Figure 2.1b shows the quartic $WWZZ$ or $WW\gamma\gamma$ coupling. Figure 2.1c shows the trilinear WWZ or $WW\gamma$ coupling. There are no all neutral vertices [8].

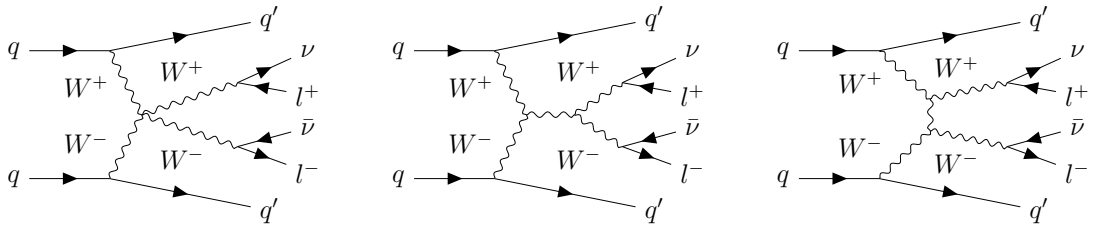

(a) (b) (c)

Figure 2.2: Feynman diagrams that contribute to W^+W^- VBS. Figure 2.2a shows the quartic interaction. Figure 2.2b shows the s-channel, and Figure 2.2c shows the t-channel [9, 10].

There are no all-neutral multi-boson interactions in the SM [3].

Vector boson scattering (VBS) is a Standard Model process where incoming quarks radiate two vector bosons which then interact and emit two new vector bosons [1, 2]. This is depicted in Figure 2.2 [9] with a quartic vertex interaction, and with the cubic coupling s-channel and t-channel contributions. After scattering, the bosons decay according to their SM couplings [6]. Opposite sign WW VBS is investigated in the leptonic decay channels where the W bosons decay to opposite charge leptons and neutrinos by ATLAS [9] and CMS [10]. The final state from this decay channel is two jets, two oppositely charged leptons, and two neutrinos [9, 10]. At leading order (LO), W^+W^- VBS is purely an electroweak process, meaning the jets are related to EWK interactions rather than QCD interactions. Vector boson scattering is a result of the triple and quartic gauge interactions. Electroweak VBS is a tool to study EWK symmetry breaking [8, 11, 12].

The W boson gains mass, and therefore a longitudinal polarization, from the Higgs

mechanism [3]. These polarizations lead to terms in the matrix elements that increase with energy, $E = \sqrt{s}$ [3]. The amplitudes of the matrix elements formed from the interactions in the Lagrangian terms Eq. (2.16) and Eq. (2.17) grow proportionally to E^4 and E^2 [11]. When Eq. (2.16) and Eq. (2.17) are summed, the E^4 terms cancel leaving just the E^2 [11]. At high energies, the cross-section will diverge. However, if the matrix elements from Eq. (2.18) (which contribute s- and t- channel diagrams) are added, the E^2 contributions are also cancelled and unitarity is preserved at high energy [3]. This cancellation is sensitive to the Higgs boson mass and makes VBS an exceptional probe into EWK symmetry breaking and BSM physics that could impact the Higgs boson.

There are other electroweak processes that contribute the same production signal but are not VBS [11]. However, VBS diagrams cannot be isolated in a gauge invariant way since quartic gauge couplings are divergent without the Higgs term contributions and therefore VBS is not directly observed [11]. Instead, a VBS enhanced region of EWK W^+W^-jj phase space is studied by ATLAS and CMS [9, 10]. The measurement that includes W^+W^- VBS is referred to as Standard Model opposite sign electroweak WW production in association with two jets (EWK W^+W^-jj). Opposite sign WW VBS refers to the diagrams where opposite sign W bosons are radiated from two incoming quarks, interact, and emit two opposite sign W bosons, examples are shown in Figure. 2.2 [11].

2.4 VBS Event Topology and Background Sources

The scattering of two same sign W bosons [13, 14] and scattering processes involving $W^{\pm}Z$ [15, 16], $W\gamma$ [17, 18], $Z\gamma$ [19, 20], or ZZ [21, 22] have been studied in the past at the LHC by the ATLAS and CMS collaborations. The scattering of two opposite sign W bosons has only recently been observed at the LHC [9, 10]. This is due to large backgrounds such as top–antitop pair production and strong W^+W^-jj production. Drell-Yan lepton production and Higgs boson-mediated WW production are other background processes.

2.4.1 QCD Backgrounds

QCD-induced W^+W^-jj events, such as the example shown in Figure 2.3, have the final state mediated via gluons [10]. The cross-section for diagrams from QCD induced W^+W^-jj have a factor of α_S^2 while the EWK W^+W^-jj diagrams are proportional to α^2. Since $\alpha_S^2 > \alpha^2$, the rate for QCD production is much greater than for electroweak production [23, 11]. These events are minimized in signal regions by kinematic selection cuts since they have different kinematic properties compared to EWK production [9, 10]. The jets from EWK W^+W^-jj

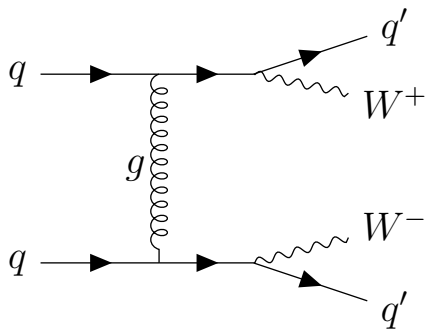

Figure 2.3: An example Feynman diagram of a process that contributes to strong W^+W^-jj production [9].

have large momentum perpendicular to the direction of the incoming quarks as a result of the quarks getting a boost from the radiated W bosons [9]. Colour confinement results in close jets at a large angle from the beamline in strong production [24]. Conversely, in electroweak production, the incoming quarks are not deterred much when they radiate the boson and so remain in line with the beam. There is one forward jet and one backward jet with a large rapidity gap between them. There is no hadronic activity within the gap [9, 24]. QCD-induced W^+W^-jj backgrounds are therefore reduced by requiring high energy, well separated jets.

2.4.2 Top Pair Backgrounds

The dominant decay mode for top quarks is $t \to W^+ b$, and then the W boson decays either hadronically or leptonically [6]. If a top–antitop pair is created, they can decay to two, oppositely charged W bosons and bottom quarks. This leads to a background source for VBS when the daughter W bosons decay leptonically. The signature for this background is two oppositely charged leptons, two neutrinos, and two jets containing bottom quarks (b-jets). Top–antitop background can be reduced by rejecting events associated with b-jets.

2.4.3 Drell-Yan and Other Backgrounds

Drell-Yan (DY) events are when a quark and antiquark annihilate and create a virtual photon or Z boson which then decays into a pair of same flavour, oppositely-charged leptons [5]. Drell-Yan does not produce neutrinos or jets at leading order. The process is shown in Figure 2.4. Drell-Yan events plus jets can leave a detector signature of two oppositely charged, same flavour leptons and two jets. The jets can arise from higher-order processes or from

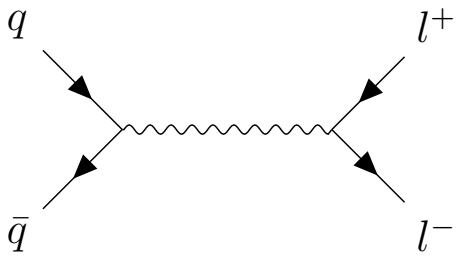

Figure 2.4: Drell-Yan production of a lepton pair [3].

other showers or radiation from initial-state quarks [10]. Higgs boson mediated W^+W^-jj production is reduced by requiring the invariant mass of the two leptons to be greater than 80 GeV [25].

To summarize, the SM is a theory that describes particles and their interactions, based on the $SU(3) \times SU(2) \times U(1)$ gauge group. The non-abelian nature of $SU(2)$ leads to self-interactions of the electroweak gauge bosons, which in turn facilitate VBS. EWK VBS observations are important probes of EWK symmetry breaking, but the measurements are difficult due to large backgrounds from QCD, top pairs, and Drell-Yan processes.

Chapter 3

Beyond the Standard Model

There is evidence that the Standard Model is not a complete model for our Universe and that there is a need for physics beyond the Standard Model (BSM). Neutrinos have now been observed to have mass while the current SM predicted them to be massless [26, 7, 6]. Observations of the rotation of stars in galaxies indicate the presence of matter otherwise not detected; this is referred to as dark matter [26, 27]. Further evidence for dark matter is found in the Cosmic Microwave Background and the Bullet Cluster [26]. The Universe is made up of more matter than anti-matter [26]. This asymmetry is not predicted or accounted for in the Standard Model [26].

Another indicator of BSM physics is the presence of fine-tuning in the current SM [3]. New physics could result in a model without the need for fine-tuning. An example of fine-tuning is within the electroweak hierarchy problem [26, 3]. The hierarchy problem arises from a sensitivity of the Higgs potential to new, massive, BSM physics [3]. If the Higgs boson couples to a heavy new particle Ψ of mass M_Ψ with strength y_Ψ, the parameter μ in the Higgs potential, Eq. (2.6), will receive a quantum correction [3]

$$\Delta\mu^2 \sim \mp\frac{y_\Psi^2}{(4\pi)^2}M_\Psi^2 \ . \tag{3.1}$$

If the new particle is a boson it is a negative correction and if it is a fermion it is a positive correction [3]. For large M_Ψ this implies $|\Delta\mu^2| >> \mu^2$ and so the quantum corrections to the Higgs boson mass would be much larger than the Higgs boson mass itself. Naturalness arguments suggest the Higgs boson mass would be same order of magnitude as the corrections. Theoretical fine-tuning can account for the discrepancy [3]. Another alternative is if there was a precise cancellation of the contributions in the high energy theory [2]. The hierarchy problem therefore motivates BSM theories that would stabilize this sensitivity.

3.1 Impact of BSM Physics on VBS

Relative to the typical parton collision centre of mass energy, new physics beyond the Standard Model could be heavy, at a scale larger than 1 TeV, or light, at a scale less than 1 TeV. Vector boson scattering production could be impacted by the effects of heavy new physics or the measurements of VBS at colliders could be contaminated by light new physics that mimics the SM VBS signal.

As described in Section 2.4, W^+W^- VBS is measured in detectors as a part of the EWK W^+W^-jj signal region with a signature of two opposite charge leptons, two jets, and two neutrinos accounted for with an imbalance of transverse momentum. Supersymmetry is one class of models that predicts new particles. In a simplified subset of models, the relevant, light new particles are called charginos and neutralinos. The charginos would decay to a stable neutralino and a SM W boson. Dichargino production with two additional jets could leave two oppositely charged leptons, an imbalance of transverse momentum from the two neutrinos and two neutralinos, and two jets, thereby faking the EWK W^+W^-jj signature. Section 3.2 provides further details on these models.

If the ultraviolet theory describing heavy BSM physics is not explicitly available, an effective field theory, described in Section 3.1.1, can be used to parameterize potential impacts on low energy, observable physics [2].

3.1.1 Effective Field Theory

Effective field theories are a method to parameterize new physics that may exist at an energy scale Λ much greater than is reachable by current experiment [2, 28]. The Standard Model has dimension $\Delta \leq 4$ operators [2]. Higher dimension operators can be written with the fields of the Standard Model and added to the SM. The EFT Lagrangian can be written as

$$\mathcal{L}_{EFT} = \mathcal{L}_{SM} + \sum_i \frac{g_i \mathcal{O}_i}{\Lambda^{\Delta_i - 4}} \,, \tag{3.2}$$

where $\mathcal{O}_i$ are operators of the effective interactions with mass dimension-Δ_i [11, 2]. The g_i are called Wilson coefficients [11]. In a model dependent interpretation, EFTs can be matched to specific BSM theories to calculate Wilson coefficients [11]. Conversely, the model independent method uses data to set limits on the Wilson coefficients for a fixed value of Λ [11]. Gravity can be incorporated into the Standard Model as a low energy EFT [29, 30].

The only gauge invariant dimension-five operator is a neutrino mass operator [11]. Dimension-six operators include four-fermion operators, new scalar couplings, and three boson opera-

tors [31]. Dimension-eight is the lowest order that permits new four boson operators [32]. Such operators would directly affect VBS processes. Higher dimension operators are suppressed compared to lower dimension operators [31]. The scale Λ indicates the scale of the new physics and could range from a TeV to the Planck scale [28]. Light new physics cannot be probed with EFTs because higher order terms in the expansion in Eq. (3.2) become important when Λ is small. EFTs have a limited range of validity; if applied at energies approaching Λ, unitarity can appear to be broken [11]. However, this is simply the result of the terms in the expansion becoming too large to ignore and the EFT approach no longer being applicable [28].

Dimension-six Wilson coefficients are constrained by precision measurements outside of VBS [33]. The terms that uniquely impact VBS in an EFT framework are of dimension-eight and are therefore suppressed. This thesis will instead focus on light new physics below the TeV scale with the use of an explicit model rather than EFT parameterizations.

3.2 Supersymmetry

One example of a specific BSM theory is supersymmetry. Supersymmetry (SUSY) is a logical theoretical extension to the Standard Model. In the SM there are fermions (quarks and leptons) and bosons (vector and scalar) [1, 2]. SUSY is a symmetry that relates fermions and bosons; every fermion would have a bosonic superpartner and every boson would have a fermionic superpartner [34, 1].

One motive for SUSY is that it could facilitate the precise cancellation needed to solve the hierarchy problem [2]. If the new particle Ψ had a superpartner $\tilde{\Psi}$, the mass correction would be

$$\Delta\mu^2 \sim \frac{y_\Psi^2}{(4\pi)^2}(M_\Psi^2 - M_{\tilde{\Psi}}^2) \ . \tag{3.3}$$

instead of Eq. (3.1). In the case of a softly broken supersymmetry, $m_{\text{soft}}^2 \sim (M_\Psi^2 - M_{\tilde{\Psi}}^2)$. If $m_{soft} \leq (4\pi/y_\Psi)\mu \leq$ TeV, SUSY would address the hierarchy problem.

A supersymmetry transformation operator Q turns a bosonic state to a fermionic state and vice versa [34]. The operator Q is a fermionic operator with spin 1/2 [34]

$$Q|\text{Boson}\rangle = |\text{Fermion}\rangle \ . \tag{3.4}$$

The Hermitian conjugate, $Q^\dagger$, is also a transformation generator [34]. For a realistic theory with chiral fermions, the following commutation and anti-commutation rules are needed for

$Q, Q^\dagger$, and the four-momentum generator P^μ [34]:

$$\{Q, Q^\dagger\} = P^\mu \tag{3.5}$$

$$\{Q, Q\} = \{Q^\dagger, Q^\dagger\} = 0 \tag{3.6}$$

$$[P^\mu, Q] = [P^\mu, Q^\dagger] = 0\ . \tag{3.7}$$

A supermultiplet is an irreducible representation of the supersymmetry algebra [34]. A supermultiplet contains fermion and boson states, these are superpartners.

An unbroken supersymmetry would have the superpartners be of the same mass as their Standard Model partners. Since the superpartners would be as discoverable as the SM particles, an unbroken supersymmetry has been ruled out experimentally by colliders predating the LHC [34, 35, 36]. A broken supersymmetry could have superparticles with different masses than their SM counterparts. Similarly to electroweak symmetry breaking, a supersymmetric model could have an exact symmetry that is spontaneously or explicitly broken by some mechanism.

3.2.1 Minimal Supersymmetric Standard Model

One approach is to explicitly break the supersymmetry by adding a symmetry-breaking term to the Lagrangian [34]. The Minimal Supersymmetric Standard Model (MSSM) is the minimal supersymmetric embedding of the Standard Model with a soft SUSY breaking [34, 26]. Softly-breaking the symmetry is done by adding a set of Lagrangian terms, $\mathcal{L}_{\text{soft}}$, containing only mass terms to the SUSY Lagrangian [34]

$$\mathcal{L}_{\text{soft}} \;=\; -\left(\frac{1}{2}M_A\lambda^a\lambda^a \;+\; \frac{1}{6}a^{ijk}\phi_i\phi_j\phi_k \;+\; \frac{1}{2}b^{ij}\phi_i\phi_j \;+\; t^i\phi_i\right) \;+\; c.c. \;-\; (m^2)^i_j\phi^{j*}\phi_i, \tag{3.8}$$

where M_A are gaugino masses for each gauge group, b^{ij} and m^2 are scalar squared-mass terms for flavour i, *c.c.* represents the complex conjugate of preceding terms, a^{ijk} is a scalar cubed coupling, and t^i is a tadpole coupling that requires ϕ to be a gauge singlet [34].

Soft breaking introduces 105 new parameters [34]. Some of these parameters predict flavour mixing and CP violation and can be constrained by corresponding measurements [34].

Before electroweak symmetry breaking in the Standard Model, there are the gauge eigenstates: one neutral B, one neutral W, and two charged W's [2]. After breaking, the bosons mix and result in the SM vector boson mass eigenstates: $W^\pm$, Z, and γ (photon) [2]. In the MSSM, the gauge eigenstates each have a fermionic superpartners called gauginos [34].

The B, W and Higgs superpartners are electroweak gauginos called binos, winos and Higgsinos [34]. After electroweak symmetry breaking, they combine into mass eigenstates: a pair of positive and negative charginos, $\chi_1^{\pm}$, and four neutralinos, χ_i^0 [34]. The lightest neutralino, χ_1^0, is assumed to be the lightest supersymmetric partner (LSP).

Matter parity, or R-parity, is a quantum number defined as

$$P_R = (-1)^{3(B-L)+2s} \tag{3.9}$$

where B is the baryon number, L is the lepton number, and s is the spin of the particle [34]. The SM particles have even R-parity, shown as $P_R = +1$. The superpartners have odd R-parity, $P_R = -1$ [34]. In a model with R-parity conservation the LSP is stable [34]. The LSP of the MSSM, χ_1^0, is stable, neutral, and weakly interacting and is therefore a possible dark matter (DM) candidate [34].

The most general gauge invariant and matter parity conserving soft supersymmetry-breaking Lagrangian term for the MSSM is:

$$\begin{aligned}\mathcal{L}_{\text{soft}}^{\text{MSSM}} = &-\frac{1}{2}(M_3\tilde{g}\tilde{g} + M_2\tilde{W}\tilde{W} + M_1\tilde{B}\tilde{B} + c.c) \\ &- (\tilde{\bar{u}}\mathbf{a_u}\tilde{Q}H_u - \tilde{\bar{d}}\mathbf{a_d}\tilde{Q}H_d - \tilde{\bar{e}}\mathbf{a_e}\tilde{Q}H_d + c.c.) \\ &- \tilde{Q}^{\dagger}\mathbf{m}_{\mathbf{Q}}^2\tilde{Q} - \tilde{L}^{\dagger}\mathbf{m}_{\mathbf{L}}^2\tilde{L} - \tilde{\bar{u}}\mathbf{m}_{\bar{\mathbf{u}}}^2\tilde{\bar{u}}^{\dagger} - \tilde{\bar{d}}\mathbf{m}_{\bar{\mathbf{d}}}^2\tilde{\bar{d}}^{\dagger} - \tilde{\bar{e}}\mathbf{m}_{\bar{\mathbf{e}}}^2\tilde{\bar{e}}^{\dagger} \\ &- m_{H_u}^2 H_u^* H_u - m_{H_d}^2 H_d^* H_d - (bH_u H_d + c.c.),\end{aligned} \tag{3.10}$$

where M_3, M_2, and M_1 are the gluino, wino, and bino masses and $\bar{u}$, $\bar{d}$, $\bar{e}$ are chiral supermultiplets [34]. Each supermultiplet represents three families, they are comprised of a complex scalar (spin-0 field) and and a left-handed two-component Weyl fermion (spin-1/2 field) [34]. Two Higgs chiral supermultiplets are required in the MSSM to prevent gauge anomalies [34]. One Higgs supermultiplet, H_u, has hypercharge $Y = \frac{1}{2}$ and couples to up type quarks [34]. The other Higgs, H_d, has hypercharge $Y = -\frac{1}{2}$ and couples to down type quarks and charged leptons [34]. In the triple-scalar coupling terms, $\mathbf{a_u}$, $\mathbf{a_d}$, and $\mathbf{a_e}$ are complex, 3×3 matrices. The squark and slepton mass terms of $(m^2)_j^i$ type include 3×3 hermitian matrices, $\mathbf{m}_{\mathbf{Q}}^2$, $\mathbf{m}_{\mathbf{L}}^2$, $\mathbf{m}_{\bar{\mathbf{u}}}^2$, $\mathbf{m}_{\bar{\mathbf{d}}}^2$, and $\mathbf{m}_{\bar{\mathbf{e}}}^2$. The Higgs terms containing $m_{H_u}^2$ or $m_{H_d}^2$ are the supersymmetry-breaking contributions to Higgs potential [34].

The MSSM scalar potential with $H_u^+ = H_d^- = 0$ is [34]

$$V = (|\mu|^2 + m_{H_u}^2)|H_u^0|^2 + (|\mu|^2 + m_{H_d}^2)|H_d^0|^2 - (bH_u^0 H_d^0 + c.c) + \frac{1}{8}(g^2 + g'^2)(m_{H_u}^2 - m_{H_d}^2)^2 \,. \tag{3.11}$$

For V to have a minimum, b and $H_u^0 H_d^0$ must be real and positive; therefore, $\langle H_u^0 \rangle$ and $\langle H_d^0 \rangle$ have opposite phases [34]. To ensure the potential is bounded from below (i.e. has a minimum), $2b < 2|\mu|^2 + m_{H_u}^2 + m_{H_d}^2$ [34]. To ensure that electroweak symmetry breaking occurs, $b^2 > (|\mu|^2 + m_{H_u}^2)(|\mu|^2 + m_{H_d}^2)$, otherwise the minimum is stable [34]. The vacuum expectation values (VEVs) can be written as [34]

$$v_u = \langle H_u^0 \rangle \ , \quad v_d = \langle H_d^0 \rangle \ , \tag{3.12}$$

with

$$\tan\beta \equiv v_u / v_d \ . \tag{3.13}$$

The VEVs are related to Z^0 and the electroweak gauge couplings through experiment [34]

$$v_u^2 + v_d^2 = v^2 = 2m_Z^2/(g^2 + g'^2) \approx (174\,\mathrm{GeV})^2 \ . \tag{3.14}$$

The term $\tan\beta$ is dependent on the Lagrangian since [34]

$$v_u = v \sin\beta \ \text{ and } \ \ v_d = v\cos\beta \ , \tag{3.15}$$

where $0 < \beta < \pi/2$ to keep the VEVs real and positive. The parameter $\tan\beta$ impacts the masses and mixing of MSSM sparticles [34]. The MSSM has two complex $SU(2)_L$ doublets which leaves 8 degrees of freedom [34]. Three degrees go to giving the Z and $W^\pm$ mass, two degrees become CP-even neutral scalars, H^0, and h^0, one degree becomes a CP-odd neutral scalar, A^0, and final two degrees become charged scalars $H^\pm$ [34]. If $m_{A^0} >> m_Z$, the particles $A^0, H^0, H^\pm$ will be heavy and near degenerate isospin doublets and decoupled from low-energy processes and leave h^0 to behave like a SM-like Higgs [34].

3.2.2 Chargino and Neutralino Mass Spectrum

Electroweak symmetry breaking leads to the Higgsinos and electroweak gauginos mixing [34]. The neutral Higgsinos, $\tilde{H_d^0}$, $\tilde{H_u^0}$, and gauginos, $\tilde{B}$, $\tilde{W^0}$, form four mass eigenstates called neutralinos, $\chi_i^0 (i = 1, 2, 3, 4)$. The indices indicate increasing mass: $M_{\chi_1^0} < M_{\chi_2^0} < M_{\chi_3^0} < M_{\chi_4^0}$. The lightest super particle is assumed to be χ_1^0 [34].

The charged Higgsinos, $\tilde{H_d^-}$, $\tilde{H_u^+}$, and gauginos, $\tilde{W^+}$, $\tilde{W^-}$, form two mass eigenstates with charge ± 1 called charginos, $\chi_i^\pm (i = 1, 2)$. The indices indicate increasing mass, $M_{\chi_1^\pm} < M_{\chi_2^\pm}$ [34].

The neutralinos in the gauge-eigenstate basis can be represented by the vector $\psi^0 =$

$(\tilde{B}, \tilde{W}^0, \tilde{H}_d^0, \tilde{H}_u^0)$ [34]. The neutralino mass terms of the Lagrangian can be written as:

$$\mathcal{L}_{M_N} = -1/2(\psi^0)^T M_{\tilde{N}} \psi^0 + c.c., \tag{3.16}$$

with $M_{\tilde{N}}$ representing the mass matrix

$$M_{\tilde{N}} = \begin{pmatrix} M_1 & 0 & -c_\beta s_W m_Z & s_\beta s_W m_Z \\ 0 & M_2 & c_\beta c_W m_Z & -s_\beta c_W m_Z \\ -c_W m_Z & c_\beta s_W m_Z & 0 & -\mu \\ s_W m_Z & -s_\beta s_W m_Z & -\mu & 0 \end{pmatrix}, \tag{3.17}$$

where $s_\beta = \sin\beta$, $c_\beta = \cos\beta$, $s_W = \sin\theta_W$, $c_W = \cos\theta_W$, and μ is the supersymmetric Higgsino mass term [34].

The mass matrix can be diagonalized with a unitary matrix $\mathbf{N}$ to obtain the mass eigenstates, $\chi_i^0 = \mathbf{N}_{ij}\psi_j^0$. The diagonalized matrix,

$$\mathbf{N}^* M_{\tilde{N}} \mathbf{N}^{-1} = \begin{pmatrix} m_{\chi_1^0} & 0 & 0 & 0 \\ 0 & m_{\chi_2^0} & 0 & 0 \\ 0 & 0 & m_{\chi_3^0} & 0 \\ 0 & 0 & 0 & m_{\chi_4^0} \end{pmatrix} \tag{3.18}$$

contains the real and positive neutralino mass terms on the diagonal; they can be written in terms of M_1, M_2, μ, and $\tan\beta$ [34]. The eigenvalues are labeled so increasing indices correspond to increasing mass.

Similarly, the chargino gauge-eigenstate basis is $\psi^\pm = (\tilde{W^+}, \tilde{H_u^+}, \tilde{W^-}, \tilde{H_d^-})$ with the chargino mass terms of the Lagrangian written as [34]

$$\mathcal{L} = -1/2(\psi^\pm)^T M_{\tilde{C}} \psi^\pm + c.c. \ . \tag{3.19}$$

The mass matrix can be written as a block matrix [34]

$$M_C = \begin{pmatrix} 0 & \mathbf{X}^T \\ \mathbf{X} & 0 \end{pmatrix} \tag{3.20}$$

with the blocks representing

$$\mathbf{X} = \begin{pmatrix} M_2 & gv_u \\ gv_d & \mu \end{pmatrix} = \begin{pmatrix} M_2 & \sqrt{2}s_\beta m_W \\ \sqrt{2}c_\beta m_W & \mu \end{pmatrix} . \tag{3.21}$$

The mass eigenstates and gauge eigenstates are related via two unitary 2×2 matrices $\mathbf{U}, \mathbf{V}$ such that

$$\begin{pmatrix} \chi_1^+ \\ \chi_2^+ \end{pmatrix} = \mathbf{V} \begin{pmatrix} \tilde{W}^+ \\ \tilde{H}_u^+ \end{pmatrix}, \quad \begin{pmatrix} \chi_1^- \\ \chi_2^- \end{pmatrix} = \mathbf{U} \begin{pmatrix} \tilde{W}^- \\ \tilde{H}_d^- \end{pmatrix}, \tag{3.22}$$

where the mixing matrix is different for the positive and negative left-handed fermions [34]. Together, U and V diagonalize X [34],

$$\mathbf{U}^* \mathbf{X} \mathbf{V}^{-1} = \begin{pmatrix} m_{\chi_1^\pm} & 0 \\ 0 & m_{\chi_2^\pm} \end{pmatrix} . \tag{3.23}$$

Most of the parameters could lead to flavour mixing or CP violation so are constrained by experiment [34]. Limitations on the lifetime of the proton is one experimental constraint [34].

Depending on the choices made for the free parameters, the resulting charginos will end up as different mixtures of the the unbroken gaugino eigenstates [34]. In the model, M_1 and M_2 refer to the masses of the bino and wino respectively. For $M_1 < M_2$ on the order of 100 GeV, χ_1^0 is bino-like and $\chi_1^\pm$ and χ_2^0 are degenerate and wino-like. This is referred to as a Bino-Wino simplified model. The mass parameters for sleptons and Higgsinos are set much larger than the wino and bino, to 1.5 TeV. The masses are set to 3 TeV for the squarks and the gluino, M_3. The heavy mass decouples the squarks, sleptons, gluinos, and Higgsinos, from the electroweakinos and simplifies the model, as in Eq. (3.2). Setting $\tan\beta = 10$ allows for a realistic Higgs boson mass [34]. The gluino mass only impacts electroweakino masses via loop corrections. Different choices of M_i, such as larger M_2 and smaller μ, could result in Higgsino-like charginos and a Higgsino-Bino model. The decay signatures of Higgsino-Bino models are similar to the Bino-Wino but with lower overall production rates. This thesis utilizes a Bino-Wino model. The masses of the binos and winos are set to cover a range of models with different chargino and neutralino masses.

3.2.3 MSSM Particle Decays

Winos and binos couple to SM particles, and so do charginos and neutralinos [34]. This thesis focuses on charginos and neutralinos because they have the potential to mimic VBS signals. Charginos and neutralinos can decay to a lighter chargino or neutralino plus a

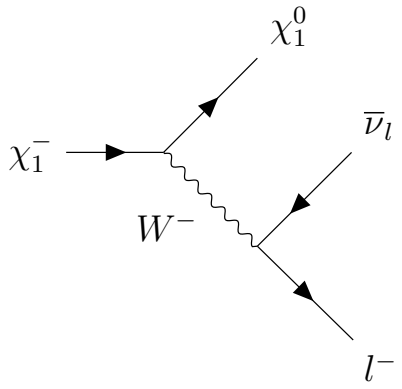

Figure 3.1: Feynman diagram depicting a chargino decay chain to a lightest neutralino and SM leptons via a SM W boson [34].

Decay Process	Branching Ratio [%]
$\chi_1^\pm \to \chi_1^0\, W^\pm$	1
$W^\pm \to e^\pm\, \nu_e$	10.71 ± 0.16
$W^\pm \to \mu^\pm\, \nu_\mu$	10.63 ± 0.17
$W^\pm \to \tau^\pm\, \nu_\tau$	11.3 ± 0.21
$\tau^\pm \to \mu^\pm\, \mu_\tau$	17.39 ± 0.04
$\tau^\pm \to e^\pm\, \nu_\tau$	17.82 ± 0.04

Table 3.1: Branching ratios relevant to the analysis including chargino decays to a neutralino and W boson, leptonic W boson decays, and τ lepton decays to lighter leptons [6].

SM EWK gauge boson (or scalar Higgs). In the Bino-Wino model, the dominant decays are $\chi_1^\pm \to \chi_1^0 + W^\pm$ and $\chi_2^0 \to \chi_1^0 + Z^0$ or $\chi_2^0 \to \chi_1^0 + h$ [34, 6]. The SM W boson then decays to SM leptons or quarks which are detectable. A decay of a chargino to a leptonically decaying W boson and lightest neutralino is shown in Figure 3.1. The lightest neutralino, χ_1^0, is assumed to be stable due to R-parity [34]. Similar to SM neutrinos, χ_1^0 is not directly detectable but could be accounted for by missing momentum in an event [5]. The final state after the decay of two oppositely charged charginos could therefore mimic the final state of opposite sign WW VBS. The decay process branching ratios are summarized in Table 3.1.

3.2.4 Current SUSY Exclusion Bounds

ATLAS and CMS publish statistical combinations of completed SUSY searches [37]. These combinations include two dimensional plots showing the exclusion zones for different chargino and neutralino masses, as shown in Figure 3.2 from ATLAS.

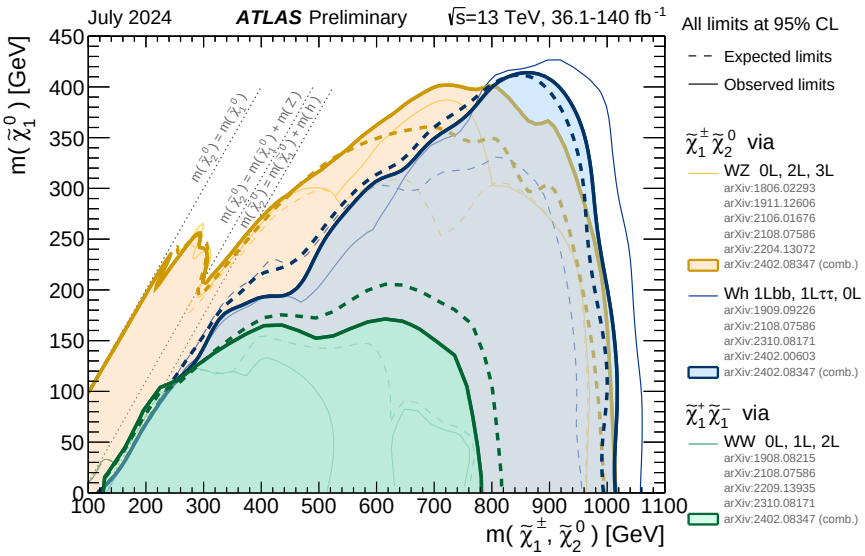

Figure 3.2: ATLAS summary plot of SUSY exclusion bounds reproduced from the SUSY summary paper [38]. The strongest current limits for $M_{\chi_1^\pm} < 800\,\text{GeV}$ charginos come from the WZ decay channel. The Wh channel gives stronger limits for $M_{\chi_1^\pm} > 800\,\text{GeV}$.

For a given MSSM model, different final states can be used to probe the same underlying model. This thesis considers opposite sign charginos so the decay mode of interest is two opposite sign W bosons. The process is shown in Figure 3.3. Other signals to consider could come from chargino neutralino production with decay modes of either WZ or Wh.

Electroweak SUSY processes have low production cross-sections, and thus they are tricky to measure at the LHC luminosity limit [37]. The strongest current bounds come from QCD production.

Though the final states can look similar to VBS, SUSY specific searches select events with different attributes. Event selection criteria include large lepton invariant mass ($m_{ll} > 100\,\text{GeV}$) to reduce low mass resonances and large missing transverse energy ($E_\text{T}^\text{miss} > 110\,\text{GeV}$) to encompass the stable lightest neutralino. Fully hadronically decaying boson searches require four jets, where two can be b-jets, and no leptons. Another case is for one boson to decay leptonically while the other decays hadronically. The signature is then one lepton, missing energy, and up to three jets with at least one high energy jet. As for SM EWK W^+W^-jj, $t\bar{t}$ is also a source of background for dichargino production.

The irregularities in the exclusion plot shown in Figure 3.2 appear where the SM Z and W bosons are produced off-shell. If the mass gap between the LSP and chargino is small, the mass spectra is considered compressed [39].

Searches have historically been done in phase space regions to minimize the SM WW

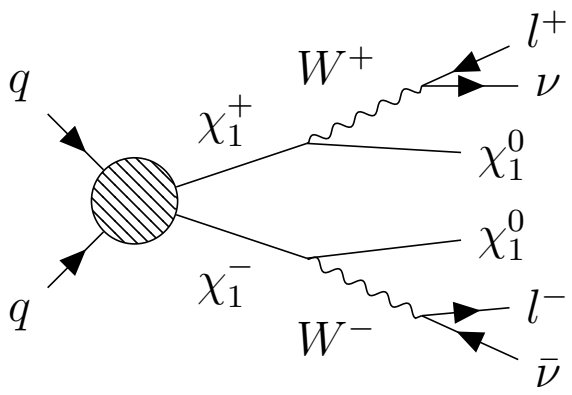

Figure 3.3: Dichargino production with decays to SM leptons through a SM W boson [40]. The final state contains $l^+,\ \nu,\ \chi_1^0,\ l^-,\ \bar{\nu},\ \chi_1^0$.

background [37]. Deliberately looking in a region designed to select for EWK W^+W^-jj gives a well measured SM background and an unexplored region of SUSY phase space. The presence of two leptons and two jets is not a typical EWK SUSY requirement. However, ATLAS performed a search for compressed SUSY using vector boson fusion topology which includes two jets but no leptons [41].

3.3 SUSY Mass Point Selection

The SUSY exclusion plot from ATLAS shown in Figure 3.2 was used as a guide to select various Bino-Wino SUSY mass points. The ATLAS plot was chosen over the plot from CMS as it compiled more dichargino searches which are most relevant [42].

3.3.1 SoftSusy

SoftSusy is a program used to calculate mass spectra of superparticles in the CP-conserving MSSM based on user-set values for SUSY parameters [43]. The mass points were calculated with SoftSusy using the flavour violating MSSM model [43]. The (renormalization) scale is set to $Q = 1.5\,\text{TeV}$. The terms $M_1,\ M_2,\ M_3$ are the bino, wino, and gluino masses, and $\mu = 1200\,\text{GeV}$ is the symmetric Higgsino mass term. The masses $M_1,\ M_2$ are varied between $0 - 1000\,\text{GeV}$; M_3 is set to 3 TeV; the squark and slepton masses are set to $2.5 - 3\,\text{TeV}$, and $\tan\beta = 10$. Due to mixing, $M_1,\ M_2 \neq \tilde{\chi}_1^0,\ \tilde{\chi}_1^\pm$ but are adjusted via trial and error to give the desired chargino masses within ± 5 GeV.

Points are chosen with $M_{\tilde{\chi}_1^\pm} > (M_{\tilde{\chi}_1^0} + M_{W^\pm})$ to ensure decays to on-shell W bosons;

off-shell decays result in small signal cross-sections. Evenly spaced points along the yellow boundary curve in Figure 3.2 were chosen from $M_{\tilde{\chi}_1^\pm} = 300\,\text{GeV}$ to $M_{\tilde{\chi}_1^\pm} = 700\,\text{GeV}$. A selection of points with fixed $M_{\tilde{\chi}_1^\pm}$ ($M_{\tilde{\chi}_1^0}$) and varied $M_{\tilde{\chi}_1^0}$ ($M_{\tilde{\chi}_1^\pm}$) were also studied. Points along $M_{\tilde{\chi}_1^0} = 250\,\text{GeV}$ are taken, starting at $M_{\tilde{\chi}_1^\pm} = 330\,\text{GeV}$ up to $M_{\tilde{\chi}_1^\pm} = 1100\,\text{GeV}$ to traverse the entire boundary. The current measurement of the SM W mass is $M_{W^\pm} = 80.3692 \pm 0.0133\,\text{GeV}$ so if $M_{\tilde{\chi}_1^0} = 250\,\text{GeV}$, charginos with mass $M_{\tilde{\chi}_1^\pm} > 330\,\text{GeV}$ can decay to on-shell W bosons [6]. The region around $M_{\tilde{\chi}_1^\pm} \approx 300\,\text{GeV}$ is more densely sampled; the irregular exclusion border and transition to off-shell W bosons is a point of interest. The line of constant neutralino mass, $M_{\tilde{\chi}_1^0} = 250\,\text{GeV}$, was chosen to intersect the rough border in Figure 3.2.

Three points along $M_{\tilde{\chi}_1^\pm} = 300\,\text{GeV}$ are taken, starting at $M_{\tilde{\chi}_1^0} = 1\,\text{GeV}$ up to $M_{\tilde{\chi}_1^0} = 200\,\text{GeV}$. They were chosen to traverse the irregular exclusion border up to the on-shell W boundary and intersect the fixed $M_{\tilde{\chi}_1^0}$ line. The distribution of mass points is shown in Figure 3.4.

Points along a line of constant $M_{\tilde{\chi}_1^\pm}$ with varied $M_{\tilde{\chi}_1^0}$ checks the impact of varying the mass splitting on the resulting cross-section. Increasing $M_{\tilde{\chi}_1^0}$ increases the missing energy in the detector signal. Points along a line of varied $M_{\tilde{\chi}_1^\pm}$ with constant $M_{\tilde{\chi}_1^0}$ checks if the cross-section changes smoothly with a change in production. Increasing $M_{\tilde{\chi}_1^\pm}$ reduces the overall production. Smooth and continuous changes allow more confident interpolation between computationally expensive sampled points.

The point $M_{\tilde{\chi}_1^0} = 1\,\text{GeV},\ M_{\tilde{\chi}_1^\pm} = 150\,\text{GeV}$ is tested as a control. The lighter masses yield higher production rates. The lighter mass points have been excluded by multiple searches so it provides a benchmark comparison for current bounds and the strength of bounds obtained in this thesis using VBS data [37].

In summary, the SM is not complete. Supersymmetry is one example of a BSM extension. The MSSM is a specific SUSY model that predicts new particles, including charginos and neutralinos that could mimic the SM EWK VBS signal. A selection of SUSY mass points are chosen, based on current ATLAS exclusion data, to examine the potential impact of SUSY on SM VBS measurements.

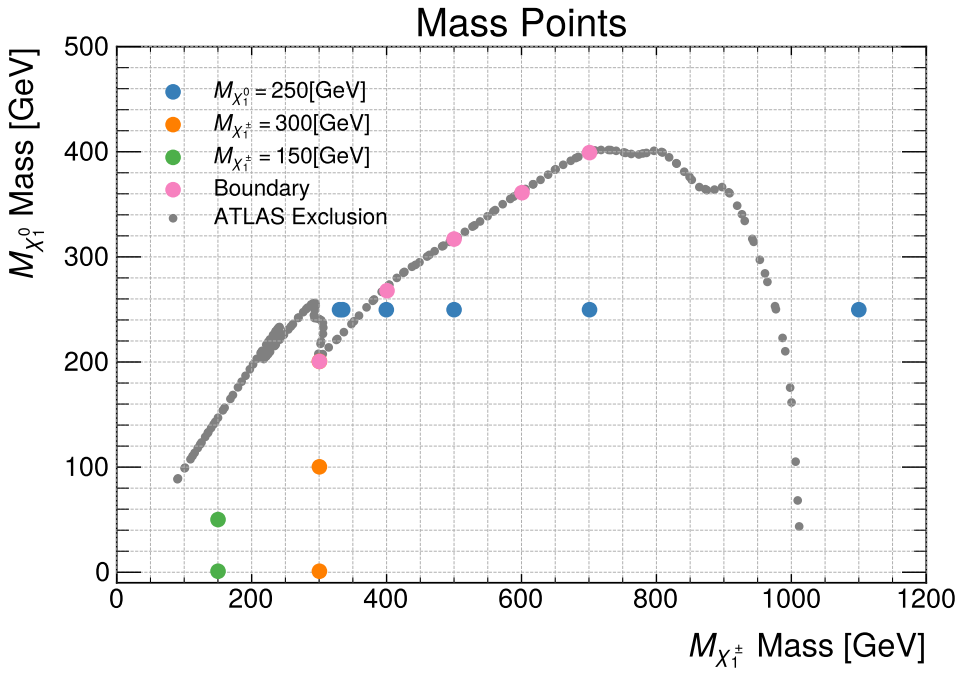

Figure 3.4: The plot shows the distribution of the chosen SUSY mass points. The x-axis represents the mass of the chargino ($M_{\chi_1^\pm}$) and the y-axis represents the mass of the lightest neutralino ($M_{\chi_1^\pm}$). The colors correspond to sets of points with fixed chargino or neutralino mass, or the set of points chosen to follow the ATLAS exclusion boundary in Figure 3.2 and [37]. The exclusion boundary shown in gray is reproduced from [44].

Chapter 4

Monte Carlo Event Generation

An event in a particle collider is the collision of two particles or the decay of a single particle and the outcome [45]. Collider events can be simulated with numerical tools to make predictions for the SM or other theories [45]. Simulated events can serve as a theoretical prediction and can be used to compare to real data.

The goal of this thesis is to evaluate potential contamination to Standard Model EWK W^+W^-jj measurements from light new BSM particles predicted with MSSM models. Two signal regions are considered, one according to the fiducial region defined by ATLAS in [9] and a second according to the fiducial region defined by CMS in [10]. First, the experiments for ATLAS and CMS with SM EWK W^+W^-jj are simulated to ensure correct set up of event generation and analysis. The analysis is then applied to simulated light BSM particle production based on a Bino-Wino simplified MSSM theory described in Chapter 3.

4.1 Event Simulation

A hard process is the term referring to a process with large energy, specifically a large momentum transfer [5, 1]. For hard processes, which are defined by an energy scale greater than the QCD confinement scale, perturbation theory is valid and Feynman diagrams can be used to calculate cross-sections; this property is called asymptotic freedom [5, 1]. Alternative methods are needed to study softer, lower energy, collinear, processes where α_s is strong and perturbation theory is no longer valid [1]. The event simulation pipeline starts with modeling the hard process with MadGraph5_aMC@NLO [46], followed by the parton shower with Pythia8 [45], then the detector response with Delphes [47], and is concluded by applying the selection criteria for the desired signal region.

4.1.1 MadGraph

MadGraph5_aMC@NLO(v3.4.2) is a Monte Carlo event generator [46]. A model is created based on the Lagrangian for some theory and is used to compute tree-level and NLO cross-sections from the matrix elements. It simulates the hard-process and generates Feynman diagrams for every sub-process that contributes to the user-defined process. The user can also define the parameters for the model used in the generation. In the parton model, quarks and gluons within a proton are called partons [3]. Different parton distribution functions (PDF) can be used [3, 46].

4.1.2 Pythia

MadGraph5_aMC@NLO is only accurate for calculating the hard process. After the hard process, partons will continue to radiate new quarks and gluons in a fractal manner; this is simulated with probabilistic algorithms called parton showers [45]. Hadronization is the process through which the outgoing partons are combined into colourless hadrons [45]. Pythia8 is used to simulate the parton showers and hadronization [45]. MadGraph is accurate for simulating hard, well separated jets while Pythia8 is superior for soft, collinear jets [45]. Pythia8 also simulates the decays of unstable particles produced in the hard process.

4.1.3 Delphes

Delphes is a software program that emulates detector responses for Monte Carlo events. It can model any axially symmetric, cylindrical, layered detector [47]. The settings can be set to emulate CMS or ATLAS specifically [47]. Detector independent physics objects are stored as well which are used to compare to unfolded, fiducial measurements [47].

The missing transverse energy $E_{\mathrm{T}}^{\mathrm{miss}}$ (MET) is an important measure used in accounting for particles that do not interact with the detector such as neutrinos or possible BSM particles [5]. Initial state partons in a collision have negligible transverse momentum, p_{T}, momentum perpendicular to the beamline [5]. The missing transverse energy is the magnitude of the missing transverse momentum, $\vec{p}_{\mathrm{T}}^{\mathrm{miss}}$ [9]. The missing transverse momentum is calculated from the negative vector sum of the transverse components of the momenta of all visible final state particles [48, 49].

Generated jets are the equivalent of truth level jets, there are no detector simulation effects [47]. They are clustered from generator level long-lived particles after parton-shower and hadronization with Pythia8 [47]. Heavy flavour jets are jets from the hadronization

of heavy flavour quarks such as bottom quarks [5]. In DELPHES-3.5.0, a potential b-jet is identified if a bottom quark is within a cone of some specified solid angle, ΔR, of the jet [47]. The probability of it being tagged as a b-jet is given by user-defined b-tagging efficiency [47].

Each MC event is given a nominal weight, and a weight for each systematic variation (PDF sets, scale choices, parton-shower variations, ect) described in Section 5.4.

DELPHES stores the truth information in the ROOT tree in branches called Particle, GenJet, and GenMET. The weights used in the systematic calculations are in a branch Weights.

4.2 Comparison of Simulation to LHC Measurements

4.2.1 Detectors

The Large Hadron Collider (LHC) is a proton-proton collider in Geneva, Switzerland [50]. It is a 27 km ring. ATLAS (A Toroidal LHC ApparatuS) and CMS (Compact Muon Solenoid) are two multipurpose detectors on the LHC [51, 50].

ATLAS Detector

ATLAS is a forward-backward symmetric cylindrical detector [51]. The symmetry is necessary as the LHC collides protons which are identical particles, as opposed to colliders that use particle and anti-particle pairs such as electrons and positrons. It has almost 4π solid angle coverage, except for the beamline itself [51]. It is constructed as a 44 m long, 25 m diameter cylinder around the beam axis plus two end-caps perpendicular to the beam [51]. The inner detector (ID) tracks charged particles with silicon pixels and microstrips [9]. It is surrounded by a transition radiation tracker to help with electron identification [51]. A solenoid makes a 2 T axial magnetic field to bend charged particles before the electromagnetic calorimeter (ECAL) made of lead and liquid argon (LAr) [51]. The barrel hadronic calorimeter (HCAL) is made of steel and scintillator-tiles while the end-caps are more LAr. The muon spectrometer is made of three air-core toroidal magnets (one surrounding the barrel, and one on each end-cap) each made of eight coils with magnetic field integrals from 2.0 to 6.0 Tm, and tracking chambers [51]. A two-level trigger system selects events [9]. The first level is hardware based and accepts events at a rate below 100 kHz [9]. The second level is software based and accepts events at a rate of 1 kHz [9].

CMS Detector

CMS is a 21 m long, 15 m diameter detector [50]. Rather than the toroidal magnets of ATLAS, it is comprised of a 6 m internal diameter solenoid that creates a 3.8 T magnetic field [14]. Within the solenoid are the silicon pixel and strip trackers, the ECAL made of lead tunstate crystal, and the HCAL made of brass and scintillators [50]. There is a steel flux-return yoke outside the solenoid that contains gas-ionization chambers for detecting muons [14]. The two-tiered trigger system uses hardware and software. The first level is comprised of hardware that uses calorimeter and muon detector information to accept events at 100 kHz [14]. The second level is a high-level trigger that runs event reconstruction software and accepts events at 1 kHz to data storage [14].

Both ATLAS and CMS reconstruct events from the information in each detector layer. Tracks are the charged-particle trajectories and vertices are the origins of a particle; they are reconstructed from hits or signals in the detector [5]. ECALs measure energy of electromagnetic showers (mainly electrons and photons) and HCALs measure the energy of QCD showers [5]. The energy and direction of particles is determined from the cluster of energy left in a group of cells [5]. The magnetic fields cause charged particles to leave curved tracks in tracking chambers [5]. The curvature gives information on the charge and momentum; positive and negative charged particles will curve in opposite directions and particles with more momentum will travel in a straighter path [5]. Muons are detected in the special muon tracking layer [52]. Neutrinos leave the detector with no interactions and are interpreted as missing transverse energy [5].

4.2.2 Measurement Unfolding

Unfolding is the process of taking a reconstructed detector measurement and translating it to a particle-level measurement [5]. This removes detector dependencies and allows for results to be compared across experiments. The fiducial region represents an area of phase space that is similar to the reconstructed region and therefore model independent [53]. Additionally, the detector inefficiencies are accounted for [5]. A fiducial cross-section is the signal cross-section for the fiducial region [5]. The ATLAS and CMS EWK W^+W^-jj studies report fiducial cross-sections [9, 10]. With detector effects minimized, the cross-section can be compared to truth level simulations. Truth level refers to particle-level Monte Carlo simulated events [5].

Chapter 5

Simulation of LHC VBS Searches

ATLAS and CMS have both recently released measurements of EWK W^+W^-jj at the LHC [9, 10]. The two searches have differently defined signal regions and therefore require separate analyses. The simulation process and selection criteria application is detailed in this section.

5.1 LHC VBS Measurement

ATLAS and CMS chose to study slightly different phase spaces. Most notably, CMS allows same flavour opposite sign lepton pairs whereas ATLAS selects for opposite flavour and opposite sign only [9, 10].

5.1.1 ATLAS

The ATLAS Collaboration measured an observation of electroweak production of oppositely charged W bosons in association with jets with a significance of 7.1σ [9]. The goal of the measurement was to check the consistency of the SM prediction of the triple and quartic gauge couplings found in VBS. Due to the close ties between VBS and electroweak symmetry breaking, deviations would indicate the EWK sector description in the SM needed updating. The unfolded fiducial cross-section is $2.7 \pm 0.5\,\text{fb}$ [9]. The theoretical prediction made using POWHEG is $2.20^{+0.14}_{-0.13}\,\text{fb}$ [9]. The prediction and measurement were in agreement. However, the measurement has an 18.5% uncertainty. The sources of uncertainty are reproduced from [9] and listed in Table 5.1. The dominant contributions are statistical uncertainties. A neural network was used to separate the signal from the large $t\bar{t}$ and strong W^+W^-jj background. This is made possible due to the distinct kinematic properties of the different processes. The $t\bar{t}$ background is modeled with simulation and constrained with a control region (CR) defined by requiring leading b-jet. Strong W^+W^-jj does not have a dedicated

Sources	$\frac{\sqrt{(\Delta\mu)^2-(\Delta\mu')^2}}{\mu}$ (%)
Monte Carlo statistical uncertainty	7.7
Top quark theoretical uncertainties	6.3
Signal theoretical uncertainties	5.8
Jet experimental uncertainties	4.9
Strong W^+W^-jj theoretical uncertainties	1.3
Luminosity	0.8
Mis-identified lepton uncertainty	0.5
b-tagging	0.4
Lepton experimental uncertainties	0.1
Others	0.3
Data statistical uncertainty	12.3
Top quark normalisation uncertainty	4.9
Strong W^+W^-jj normalisation uncertainty	2.2
Total uncertainty	**18.5**

Table 5.1: Uncertainty breakdown table reproduced from ATLAS EWK W^+W^-jj measurement [9]. The statistical data uncertainty is the largest contributor.

CR as it is too similar to $t\bar{t}$. The normalisation of simulated W^+W^-jj is floated in the profile likelihood fits in the CR and signal region (SR).

5.1.2 CMS

The CMS collaboration measured electroweak production of oppositely charged W bosons in association with exactly two jets with a significance of 5.6 standard deviations [10]. The measured fiducial cross-section is 10.2 ± 2.0 fb while the theory prediction is 9.1 ± 0.6 fb [10]. The measurement has a 19.8% uncertainty. The sources of uncertainty are reproduced from [10] and listed in Table 5.2; the data statistical uncertainty is the largest source of uncertainty. The measurement was done to probe the Higgs sector. Additionally, the measurement can be used to constrain EFT parameters by determining dimension-six operators. CMS includes same flavour lepton pairs in the signal region so Drell-Yan production is a major source of background. The control region for Drell-Yan is defined near the Z boson peak. A deep neural network is used to extract the VBS signal from the $t\bar{t}$ and QCD background. The signal was simulated at leading order with MADGRAPH and PYTHIA8.

Uncertainty source	**Value**
QCD-induced W^+W^- normalization	5.3%
$t\bar{t}$ scale variation	5.1%
VBS signal scale variation	5.0%
$t\bar{t}$ normalization	4.9%
b tagging	3.5%
Trigger corrections	3.3%
DY normalization	2.9%
Jet energy scale + resolution	2.6%
Unclustered $p_{\mathrm{T}}^{\mathrm{miss}}$	2.4%
QCD-induced W^+W^- scale variation	2.1%
Integrated luminosity	2.0%
Muon efficiency	2.0%
Pileup	1.8%
Electron efficiency	1.5%
Underlying event	1.3%
Parton shower	1.0%
Other	$< 1\%$
Total systematic uncertainty	**13.1%**
Total statistical uncertainty	**14.9%**
Total uncertainty	**19.8%**

Table 5.2: Uncertainty breakdown table reproduced from CMS EWK W^+W^-jj measurement [10]. The statistical data uncertainty is the largest contribution.

5.1.3 Comparison of ATLAS and CMS Results

The signal regions are defined by selection criteria on kinematic variables and observables. Pseudorapidity, η, is a measure of the direction of a particle based on the angle between the beam axis and a particle or jet,

$$\eta \equiv -\ln\left(\tan\left(\frac{\theta}{2}\right)\right), \tag{5.1}$$

where θ is the angle between the three-momentum and the beam axis [5]. Pseudorapidity is positive for particles or jets near the forward beamline, zero for perpendicular particles, and negative near the backwards beamline. Angular separation is measured with

$$\Delta R = \sqrt{(\Delta\eta)^2 + (\Delta\phi)^2}, \tag{5.2}$$

where $\Delta\eta$ is the difference in pseudorapidity between two elements and $\Delta\phi$ is the difference between the angles in the transverse plane between the two elements [10]. Leptons are dressed with photons in a cone of radius $\Delta R = 0.1$. A dressed lepton is a bare lepton with the four-momentum of photons within $\Delta R < 0.1$ added to its four-momentum. Jets are clustered with the anti-k_t algorithm with radius parameter $R = 0.4$. The anti-k_t algorithm utilizes rapidity, $y = \frac{1}{2}\ln\frac{E+p_z}{E-p_z}$, rather than pseudorapidity in the angular separation definition because jets have mass.

Centrality, ζ, is a measure of the relative positioning of leptons and jets in an event,

$$\zeta = \text{centrality} = \min\left([\min(\eta_{l1},\eta_{l2}) - \min(\eta_{j1},\eta_{j2})], [\max(\eta_{j1},\eta_{j2}) - \max(\eta_{l1},\eta_{l2})]\right), \quad (5.3)$$

where $\eta_{j1(2)}$, $\eta_{l1(2)}$ are the leading (sub-leading) jet and lepton pseudorapidities [9]. The first term represents $\Delta\eta$ of the backwards lepton and jet, while the second term is $\Delta\eta$ of the forward lepton and jet. Typical EWK W^+W^-jj events tend to have positive centrality due to the jets being more parallel to the beamline and the leptons being more transverse to the beamline [9]. If $\zeta < 0$ it would mean one of the jets and leptons had swapped places with respect to the expected topology. Requiring $\zeta > 0.5$ selects for events where the jets and leptons are more separated and enhances signal to background ratio.

As stated in Subsection 2.4.1, compared to QCD-induced W^+W^-jj, EWK W^+W^-jj produces high energy, well separated jets. The EWK W^+W^-jj events are selected for by requiring large dijet invariant mass, m_{jj}, and large jet transverse momentum, p_{T} [9, 10]. Separation of the jets is deemed by either the difference in jet pseudorapidity Eq. (5.1), $|\Delta\eta_{jj}|$, as is done at CMS, or with the centrality Eq. (5.3), ζ, as is done at ATLAS.

Neutrinos are not detected by ATLAS or CMS; they are accounted for with E_T^{miss}. Drell-Yan (DY) events as described in Section 2.4.3, do not produce neutrinos and are reduced by requiring missing transverse energy E_T^{miss} [9, 10]. Selecting opposite flavour leptons can further reduce the background as Drell-Yan only makes same flavor pairs. However, there will still be a portion of Drell-Yan events where a pair of τ leptons are created and decay to opposite flavor light leptons and neutrinos, $\tau^+\tau^- \to \mu\ e\ \nu_\tau\ \bar{\nu}_\tau\ \nu_\mu\ \nu_e$ [10]. Requiring jets in the final state also reduces DY background events since they does not produce jets at leading order. CMS looks at a larger area of phase space, including same flavour opposite sign leptons [10]. In the case of same flavour lepton events, the Drell-Yan background is controlled only with E_T^{miss} in the same flavour channels [10]. Electrons and muons from τ decays are vetoed by CMS in the fiducial region [10].

If a top antitop pair is created, they can decay to oppositely charged W bosons and

bottom quarks [6]. The dominant decay mode for top quarks is $t \to W^+ b$ [6]. Events with at least one b-jet are discarded to suppress background processes with top quark decays [9].

Higgs mediated W^+W^-jj production is reduced by requiring the invariant mass of the two leptons to be greater than 80 GeV [9, 10]. A large dijet invariant mass, m_{jj}, requirement suppresses triboson events and strong production of W^+W^-jj. Negligible same sign W pairs are present with the aforementioned selection criteria.

The key differences between the ATLAS and CMS fiducial regions are the required number and flavours of leptons, dijet invariant mass, jet energy, and how the angular separation of jets and leptons is quantified. CMS allows an additional lepton if it has low p_{T}, same flavour lepton combinations, and lower dijet invariant mass, but requires harder jet p_{T}. CMS determines the angular separation of jets and leptons with $\Delta\eta_{jj}$ and $\Delta R\,(l,\ j)$. This ensures jets are well separated and the leptons are distinct from the jets. ATLAS uses the centrality which selects for the expected VBS topology of two well separated jets with lepton between them. The selection criteria is summarized in Table 5.3.

5.2 Standard Model VBS Simulation

Standard Model opposite sign electroweak WW in association with two jets (EWK W^+W^-jj) production is simulated with MadGraph5_aMC, Pythia8, and Delphes. Opposite sign WW VBS refers to the processes where opposite sign W bosons are radiated from two incoming quarks, interact via the quartic coupling, and emit two opposite sign W bosons. In the channel of interest, the W bosons then decay leptonically, $W^\pm \to l^\pm + \nu_l$ [9, 10]. In [10], CMS looked for W bosons decaying to any combination of opposite sign light leptons; τ leptons and decays from τ leptons are not included. While in [9], ATLAS exclusively looked at W bosons decaying to opposite flavor and opposite sign leptons and τ leptons and decays from τ leptons are included. The final state that is simulated is two jets, two opposite charged leptons, and two neutrinos (Figure 2.2).

As mentioned in Section 2.3, VBS is not directly observed in isolation as the quartic gauge couplings are not gauge invariant. CMS and ATLAS have their own definitions for a VBS enhanced region of EWK W^+W^-jj phase space [9, 10].

The ATLAS and CMS detectors do not detect W bosons directly, only their decay products. In this case, the detected decay products are light leptons. Tau leptons are also not detected directly, but they decay to the lighter leptons and can contribute to signal [6]. An electroweak event of two protons colliding to a final state containing two oppositely charged leptons, a neutrino, an antineutrino, and two jets, is generated in Madgraph with the

Attribute	ATLAS	CMS
$E_{\mathrm{T}}^{\mathrm{miss}}$	$> 15\,\mathrm{GeV}$	$> 20\,\mathrm{GeV}$
Lepton p_{T}	$> 27\,\mathrm{GeV}$	$p_{\mathrm{T}}^{l_1} > 25\,\mathrm{GeV}$, $p_{\mathrm{T}}^{l_2} > 13\,\mathrm{GeV}$, $p_{\mathrm{T}}^{l_3} < 10\,\mathrm{GeV}$
Lepton $\lvert\eta\rvert$	< 2.5	< 2.5
N_{Lepton}	2	2 or 3
Lepton Flavour	$e\mu$	ee, $e\mu$, $\mu\mu$
Lepton Charge	Opposite Charge	Opposite Charge
Jet p_{T}	$> 25\,\mathrm{GeV}$	$> 30\,\mathrm{GeV}$
Jet $\lvert\eta\rvert$	< 4.5	< 4.7
N_{Jet}	2 or 3	$>= 2$
b-jet p_{T}	$> 20\,\mathrm{GeV}$	-
b-jet $\lvert\eta\rvert$	$< 2.5\,\mathrm{GeV}$	-
$N_{b-\mathrm{jet}}$	no b-jet	no b-jet
m_{jj}	$> 500\,\mathrm{GeV}$	$> 300\,\mathrm{GeV}$
$\Delta\eta_{jj}$	-	$>= 2.5$
$\Delta R(l,j)$	-	> 0.4
ζ	> 0.5	-
m_{ll}	$> 80\,\mathrm{GeV}$	$> 50\,\mathrm{GeV}$

Table 5.3: A comparison of the fiducial region criteria used by ATLAS and CMS to measure EWK W^+W^-jj [9, 10]. ATLAS enforces stricter criteria on jet and lepton invariant mass, number of leptons, lepton flavor combinations, and lepton transverse momentum. CMS has stricter criteria for missing transverse energy, and jet transverse momentum. To enforce the relative lepton and jet VBS topology, ATLAS uses centrality, ζ, while CMS uses $\Delta\eta_{jj}$ and $\Delta R(l,j)$.

command

$$p\ p \to\ l_1^+\ l_2^-\ \nu_1\ \overline{\nu_2}\ j\ j\ \$\, t\ \bar{t}\ \mathrm{QED} == 6\ \mathrm{QCD} = 0\ . \tag{5.4}$$

The multiparticle $l^{\pm}$ represents the charged leptons, $l^+(l^-) = \mu^+, e^+, \tau^+(\mu^-, e^-, \tau^-)$.

Only pure electroweak Feynman diagrams are generated by setting QED to six vertices and QCD is set to zero vertices. The term $\$\, t\ \bar{t}$ forbids on-shell s-diagram top quarks [46]. Two jets are added to complete the VBS topology. For efficient generation, the lepton channels are generated separately; there is no interference between them. For example, generate $p\ p > e^+\ \nu_e\ \mu^-\ \bar{\nu}_\mu\ j\ j\ \$\ t\ \bar{t}$ QED== 6 QCD= 0, for every combination of opposite sign leptons, process through the selection criteria, and sum the resulting cross-sections. The

ATLAS	CMS
e, μ	e, μ
e, τ	e, e
μ, τ	μ, μ
τ, τ	-

Table 5.4: Lepton final states generated for each experiment. Both opposite charge configurations of the opposite flavour pairs were generated.

Process	**Events**	**Passed Events**	σ_{ATLAS} $[fb]$	σ_{CMS} $[fb]$
$p\ p \to e^-\ \overline{\nu_e}\ \mu^+\ \nu_\mu$	43792	2497	0.91 ± 0.08	2.19 ± 0.15
$p\ p \to \mu^-\ \overline{\nu_\mu}\ \mu^+\ \nu_\mu$	45832	4	0.0014 ± 0.0008	2.46 ± 0.17
$p\ p \to \tau^-\ \overline{\nu_\tau}\ e^+\ \nu_e$	29456	124	0.066 ± 0.012	–
$p\ p \to \tau^-\ \overline{\nu_\tau}\ \mu^+\ \nu_\mu$	29456	147	0.079 ± 0.013	–
$p\ p \to \tau^-\ \overline{\nu_\tau}\ \tau^+\ \nu_\tau$	80739	58	0.012 ± 0.004	–
$p\ p \to \mu^-\ \overline{\nu_\mu}\ e^+\ \nu_e$	43984	2516	0.91 ± 0.08	2.19 ± 0.16
$p\ p \to e^-\ \overline{\nu_e}\ \tau^+\ \nu_\tau$	28676	125	0.069 ± 0.010	–
$p\ p \to \mu^-\ \overline{\nu_\mu}\ \tau^+\ \nu_\tau$	28676	105	0.057 ± 0.009	–
$p\ p \to e^-\ \overline{\nu_e}\ e^+\ \nu_e$	45551	6879	–	2.46 ± 0.18
Total			2.10 ± 0.11	9.30 ± 0.28

Table 5.5: Cross-sections, σ, for each lepton channel simulated with MADGRAPH, PYTHIA, and DELPHES for ATLAS and CMS EWK W^+W^-jj signal regions [9, 10]. The number of events generated and the number of events that pass the selection criteria are listed. The uncertainties are sum of statistical and systematic uncertainties from MADGRAPH.

lepton combinations are summarized in Table 5.4. The ATLAS sample includes $e^+\mu^-$, $e^-\mu^+$, $e^+\tau^-$, $\mu^+\tau^-$, $e^-\tau^+$, $\mu^-\tau^+$, $\tau^+\tau^-$. The CMS sample requires only e^+e^-, $\mu^+\mu^-$, $e^+\mu^-$, $e^-\mu^+$ since the CMS fiducial region, events from τ leptons decays are vetoed and the samples with τ leptons are not included [10].

The MADGRAPH model "`sm-no_b_mass`" is used to set the majority of parameters for the Standard Model simulations. The Fermi coupling constant, M_t, M_Z, the decay widths for top quarks, Higgs boson, and W bosons, and the Yukawa coupling for top quarks are updated to the PDG values contemporary to the ATLAS and CMS VBS publications [54, 9, 10]. A standardized catalog of parton distribution functions (PDFs) is provided by LHAPDF6 [55]. The PDF set LHAPDF LHAID 260000 is used, `NNPDF30_nlo_as_0118`. The strong coupling constant, α_S, is set by the PDF choice. My simulated recreation of SM EWK W^+W^-jj is within the uncertainty for the theoretical cross-section for both ATLAS and CMS. Ta-

	ATLAS cross-section [fb]	CMS cross-section [fb]
Official simulation	$2.20^{+0.14}_{-0.13}$	9.1 ± 0.6
Measurement	2.7 ± 0.5	10.2 ± 2.0
This work's simulation	2.10 ± 0.11	9.30 ± 0.28

Table 5.6: Comparison of EWK W^+W^-jj simulations and measurement in ATLAS and CMS signal regions [9, 10]. The validation performed for this thesis is in agreement with both the published simulations and experimental measurements.

ble 5.6 lists the simulations and measurements for the two signal regions. ATLAS calculated $2.20^{+0.14}_{-0.13}$ fb compared to my simulated 2.10 ± 0.11 fb and CMS calculated 9.1 ± 0.6 fb compared to my simulated 9.30 ± 0.28 fb. This validates the analysis regime to be used for SUSY simulations. The results of the simulation are summarized in Table 5.5.

5.3 SUSY Simulation

The SUSY process simulated is two charginos with two jets. The simulation is repeated for various Bino-Wino SUSY models of different chargino and neutralino masses. The selection criteria from Section 5.2 is implemented.

When doing a SUSY simulation, the model `MSSM_SLHA2-full` is used [46]. The jet matching scale `xqcut` is set to 30 GeV which sets `qcut` to 45 GeV. The setting `Auto_ptj_mjj` is set to True. The parameter cards are calculated for each SUSY mass point using SoftSusy and MadGraph as described in Section 3.3.1. Due to mass mixing in the model, the choice of SUSY masses can affect the SM particle masses in the model. Therefore the parameters are not updated with the PDG values as was done in the SM simulation.

A multiparticle called `susyexclude` is defined to eliminate contrived diagrams that inhibit generation of the main chargino-chargino process. It contains gluinos, squarks, antisquarks, sleptons, and antisleptons. It leaves only the neutralinos and charginos. In the Bino-Wino model chosen, the particles in `susyexclude` are heavy and decoupled. Therefore these diagrams should not contribute meaningfully to the cross-section but they require lots of computing power.

The basic set up to run a SUSY simulation in MadGraph is:

```
import model MSSM_SLHA2-full
define susyexclude = go ul ur dl dr cl cr sl sr t1 t2 b1 b2 ul~ ur~
dl~ dr~ cl~ cr~ sl~ sr~ t1~ t2~ b1~ b2~ el- el+ er- er+
mul- mul+ mur- mur+ ta1- ta1+ ta2- ta2+ sve svm svt sve~ svm~ svt~
```

$M_{\chi_1^\pm}$ [GeV]	$M_{\chi_1^0}$ [GeV]	Events Generated
330	250	2998809
335	250	999574
400	250	999627
500	250	999641
700	250	899705
1100	250	598703
300	1	999558
300	100	999588
300	200	999566
150	1	4997518
150	50	999524
400	268	999621
500	317	999623
600	360	999674
700	400	999674

Table 5.7: Number of MADGRAPH events generated for each $(M_{\chi_1^\pm}, M_{\chi_1^0})$ mass point.

```
generate p p \> x1+ x1- /susyexclude
add process  p p \> x1+ x1- j /susyexclude
add process  p p \> x1+ x1- jj /susyexclude
```

The charginos are decayed by PYTHIA8. The `onifany` setting is used in PYTHIA8 to force any W bosons to decay via the leptonic channels. Decays of W bosons to τ leptons are included since they can further decay and fit the selection criteria. CMS's SM VBS criteria explicitly left out τ leptons, ATLAS included them. However, this analysis is focused on any manner that SUSY could infiltrate the SM VBS signal so the τ leptons are included.

The final cross-section is acquired by multiplying the simulation result by the branching ratio of W to leptons, for each W. This means the cross-section that is output from MADGRAPH is multiplied by $(\mathbf{Br}(W \to l\ \nu_l))^2 = 0.338^2$ [6]. At least 100k events per SUSY mass point were generated to minimize the impact of statistical uncertainties. Statistical uncertainties as well as systematic uncertainties are further detailed in Section 5.4.

5.4 Uncertainty Estimation

Uncertainties, also referred to as errors, can be categorized as statistical, systematic, or theoretical [56].

Statistical uncertainties are the result of random fluctuations and variations between repeated experiments. Their impact can be reduced by increasing the number of events in a sample; the relative statistical uncertainty scales by $\frac{1}{\sqrt{N_{\text{events}}}}$ [56].

Systematic uncertainties stem from unknowns and assumptions within a theory [56]. Some types of systematic uncertainties are: scale, PDF, and jet matching scale (`xqcut`). Systematic uncertainties are independent of sample size so they cannot directly be reduced by taking more data.

The systematic uncertainties can be calculated in the MC simulation by varying the scale choice or PDF [57]. Rather than regenerate MC events for each scale or PDF variation, one set of events is generated and the events are reweighted according to the scale or PDF choice. This saves computing time and eliminates statistical uncertainties between different samples, essentially isolating the effect of systematic uncertainties since sets are 100% correlated. DELPHES outputs all the reweighted MADGRAPH events in a ROOT tree [47, 58]. The labels for the weights are found in the PYTHIA8 event log. Events are processed through the analysis selection implemented with ROOT code. The passed events have their weights added to a corresponding histogram bin. The sums of weights passing the selection are what is used to calculate the uncertainties in the signal phase space.

Parton distribution functions (PDFs) describe the momentum fractions of partons within (composite) hadrons such as protons [55]. The LHC collides protons but cross-section calculations are done at parton-level with matrix elements; the choice of PDF could affect a measurement. LHAPDF (Les Houches Accord) provides PDF error sets, a set of varied parameters used to estimate the uncertainty [55]. They are either provided as a set of replicas which are used to calculate the standard deviation (Monte Carlo representation), or as the Hessian representation of a central value and covariance matrix eigenvectors [55]. Multiple PDF sets should be used to minimize bias.

This thesis used `PDF4LHC15_nlo_30` (`PDFID 90400`, which contains 30 PDF symmetric eigenvectors) and `NNPDF30_nlo_as_0118` (`PDFID` 260000, which contains 100 PDF replicas). For `PDFID` 260000, the envelope is calculated with

$$\delta^{\text{pdf}}\sigma = \sqrt{\frac{1}{N-1}\sum_{k=1}^{N}(\sigma^{(k)} - \langle\sigma\rangle)^2}\,, \qquad \langle\sigma\rangle = \frac{1}{N}\sum_{k=1}^{N}\sigma^{(k)}, \tag{5.5}$$

where N is the number of replicas not including the central PDF [55]. For `PDFID` 90400 the

envelope is calculated with [55]

$$\delta^{\text{pdf}}\sigma = \sqrt{\sum_{k=1}^{N}(\sigma^{(k)} - \sigma^{(0)})^2} \ . \tag{5.6}$$

The scale uncertainties are related to the scale factors muR, muF ($\mu_{\text{F/R}}$); renormalization and factorization scales respectively [5]. The uncertainties arise from the truncations of expansions to renormalize the strong coupling and reabsorb initial state IR-divergences [5]. The scale μ_{R} and μ_{F} are both varied individually by a factor of 0.5 and 2 [5]. Excluding the opposite extremes (0.5, 2), the six remaining combinations of variations are compared [5]. The maximum up and down deviations of the observable are taken as the scale uncertainties [5]. The scale uncertainty envelope is found by

$$\max[\mathcal{O}(\mu_{F_i}, \mu_{R_i}) - \mathcal{O}(\mu_{F_i} = 1, \mu_{R_i} = 1)] \tag{5.7}$$

for observable $\mathcal{O}$. Dynamical scale choice is another variation calculated by MG but was not incorporated.

The nominal `xqcut` value is chosen based on the stability of the djr plots and events are generated. Then `xqcut` is varied up and down by 10 GeV and events are regenerated. The maximum cross-section deviation is used as the uncertainty.

In addition to the nominal `qcut` value, events are reweighted by MADGRAPH for two larger values of `qcut`. Since the `qcut` value is based on `xqcut`, these are not taken as a separate uncertainty and are not utilized.

The separate uncertainties can be combined in quadrature [56]

$$\sigma_{\text{sys}} = \sqrt{\sigma^2_{\text{xqcut}} + \sigma^2_{\text{scale}} + \sigma^2_{\text{pdf}} + \sigma^2_{\text{pdf}}} \ . \tag{5.8}$$

The statistical uncertainty for N events is

$$\sigma_{\text{stat}} = \sqrt{N} \tag{5.9}$$

from the Poisson distribution [56]. The total uncertainty is the the statistical and systematic uncertainties added in quadrature

$$\sigma_{\text{total}} = \sqrt{\sigma^2_{\text{sys}} + \sigma^2_{\text{stat}}} \ . \tag{5.10}$$

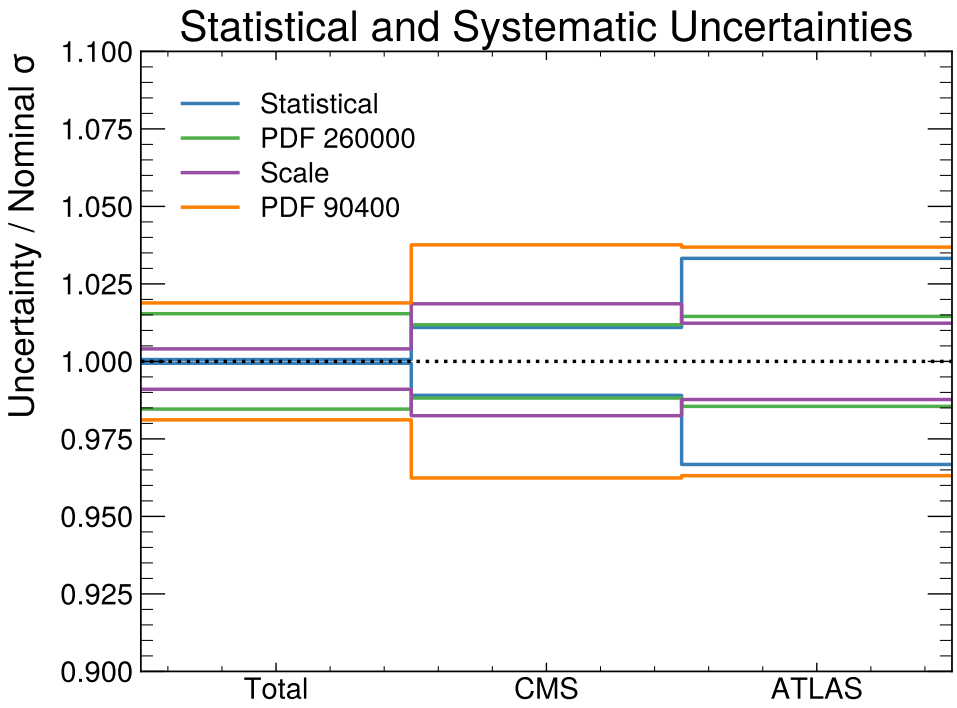

Figure 5.1: The uncertainty envelopes calculated from the reweighted MADGRAPH events for three sets: all the events generated, the events passing CMS selections, and the events passing the ATLAS selection. The uncertainties are normalized to the nominal value for each signal region. The colours represent the different uncertainties: statistical, PDF set 260000, scale, and PDF set 90400. The number of events decrease from left to right and the uncertainties become more prominent.

For a given process, enough events were generated to minimize the stat uncertainty, $\sigma_{\text{total}} \approx \sigma_{\text{sys}}$; $\sigma_{\text{sys}} >> \sigma_{\text{stat}}$. Figure 5.1 shows the systematic uncertainties and statistical uncertainty normalized to the nominal cross-section for an example mass point simulation before any selection criteria, and after CMS or ATLAS selection criteria. The statistical uncertainty is smaller than any systematic contributions for CMS. In the ATLAS signal region the statistical uncertainty is near the same order of magnitude as the systematic uncertainty. This is due to the smaller signal region and therefore fewer events for ATLAS compared to CMS.

To summarize, EWK W^+W^-jj has been measured by ATLAS and CMS. The collaborations used different definitions for their signal regions. Both sets of selection criteria were reproduced and validated with Monte Carlo event simulations of EWK W^+W^-jj. Various SUSY models were simulated and passed through both sets of selection criteria in order to

observe potential contamination. Theoretical modeling uncertainties were estimated with reweighted of events.

Chapter 6

Statistical Analysis of Results

6.1 Review of Statistical Methods

Once an expected (i.e. theoretical) result and a measured (i.e. experimental) result have been obtained, quantitative comparison of the two must be made. In this thesis, different SUSY model parameter points are tested for consistency with observation using a method of calculating confidence levels called CL_s. The method is used to compare cross-section predictions from the SUSY model simulations to published cross-section VBS measurements.

Both expected and measured results can be modeled with some probability density function (PDF[1]) [56]. For a counting experiment, this would be a simple, discrete Poisson distribution. The parameter of interest (POI) is the signal strength parameter, μ [56]. Statistical and systematic uncertainties on the measured data and the expected background are treated as nuisance parameters [56, 5]. Nuisance parameters are floated in the fits similarly to the POI, but ultimately their final value is unimportant. The expected number of events is $\mu \cdot s + b$, where s is predicted number of signal events and b is the predicted number of background events.

Hypotheses are predictions based on the value of the signal strength [56]. The null hypothesis, also called the background only hypothesis, is referred to as the $\mu = 0$ hypothesis. The nominal signal hypothesis is $\mu = 1$.

A probability density function (PDF), $f(x|\mu)$, is a function of a potential measurement, x, under some fixed hypothesis, μ [56]. The PDF is normalized to one. It is interpreted as the probability of x given μ. The function called the likelihood, $\mathcal{L}(x';\mu)$, is the PDF at a fixed, measured data point x'; it is a function of the POI, μ [56]. It is not normalized to one so it does not calculate probability rather a similar property called the likelihood. It represents the

[1]Not to be confused with parton distribution functions, which are also called PDFs. The intended definition should be clear from context.

likelihood of the hypothesis μ given the observed measurement. The maximum-likelihood estimate (MLE) gives the estimator for μ [56]. The estimator is denoted with a hat, $\hat{\mu}$. Practically, $\hat{\mu}$ is found by minimizing twice the negative log of the likelihood [56]. Calculating $\hat{\mu}$ is what is referred to as "fitting the data"; it shows what hypothesis best represents the data.

A profile likelihood ratio

$$\lambda(\mu) = \frac{\mathcal{L}(x; \mu, \hat{\hat{\theta}})}{\mathcal{L}(x; \hat{\mu}, \hat{\theta})} \tag{6.1}$$

is used when there are many nuisance parameters θ and one POI μ [59]. The nuisance parameter maximum likelihood estimator (MLE) for a specific value of μ is $\hat{\hat{\theta}}$. The global MLE are $\hat{\mu}$ and $\hat{\theta}$; they are both allowed to float when minimizing the likelihood [56]. Possible values of the profile likelihood ratio are $0 \leq \lambda(\mu) \leq 1$; values closer to 1 indicate better agreement between the data and μ. A test statistic

$$t_\mu = -2\ln(\lambda) \tag{6.2}$$

is used to compare a null hypothesis and alternate hypothesis [59]. Large values of the test statistic t_μ represent incompatibility between the data and μ.

6.1.1 Hypothesis testing

A p-value (p) of a hypothesis with signal strength μ is a measure of how often, under repeated identical experiments, a result is as or less compatible with the hypothesis than the observation [59]. The function $f(t_\mu|\mu_{\text{data}})$ is a probability density function for values of the test statistic, t_μ, calculated for some data. The data is distributed according to some "truth" $\mu = \mu_{\text{data}}$. The observed test statistic, t_{obs}, is the test statistic calculated for a measurement of the data. The p-value for a hypothesis, p_μ, is calculated by integrating the tail of $f(t_\mu|\mu_{\text{data}})$ [56]

$$p_\mu = \int_{t_{\text{obs}}}^{+\infty} dt_\mu f(t_\mu|\mu_{\text{data}}) \ . \tag{6.3}$$

A small p-value is associated with a measurement that is unlikely for the given hypothesis and suggests the construction of an alternative [56]. We can reject a hypothesis at a confidence level $\text{CL} = 1 - p_\mu$ if the p-value is deemed sufficiently small. Typically, $\text{CL} = 95\%$ is desired [56]. The associated frequentist statement is that 95% of future repeated experiments will be as or more compatible with the hypothesis as the original observation. A p-value is

often converted to a "significance",

$$Z = \Phi^{-1}(1-p) \ , \tag{6.4}$$

where Φ^{-1} is the inverse of the cumulative distribution) of the standard Gaussian. The value of Z is the number of standard deviations from the mean that a Gaussian distributed variable would be with an equivalent p-value [59]. A significance of $Z = 5\,\sigma$ indicates discovery. It is equivalent to a p-value of $p = 2.87 \times 10^{-7}$ [59]. Signal hypothesis exclusion at a 95% confidence level is equivalent to $p = 0.05$ or $Z = 1.64\,\sigma$.

Hypothesis testing is based on probability; there is potential to draw incorrect conclusions. A type I error is when the null hypothesis, H_0, is rejected when is actually true [56]. The size of the test, α, is the rate for type I errors if the data is actually distributed according the strength parameter in H_0

$$\alpha = \int_{t_c}^{\infty} f(t|H_0)dt \ . \tag{6.5}$$

A type II error is when the null hypothesis is not rejected when it is false [56]. The power of the test, β, is the rate for type II errors if there is one alternative hypothesis, H_1, and either the null or alternative are true and the data is distributed according to the alternate hypothesis

$$\beta = \int_{-\infty}^{t_c} f(t|H_1)dt \ . \tag{6.6}$$

6.1.2 CLs

In a fusion of Bayesian and frequentist approaches, the CL_s measure was designed to amplify small signals against similar background in order to set upper limits [60, 61]. The test statistic in Eq. (6.2) is a ratio comparing likelihoods for the same data under two different hypotheses: signal plus background where $\mu = \mu'$, and background only where $\mu = 0$. The CL_s measure is a ratio of confidence levels for the same hypothesis but calculated for data containing signal plus background and data containing background only.

The confidence level of an observation for a hypothesis with $\mu = \mu'$ and where the true value is $\mu = \mu'$ (the data is distributed with a strength parameter μ') is defined as [60]

$$\mathrm{CL}_{s+b} = p_{\mu'} = \int_{\tilde{q}_{\mathrm{obs}}}^{\infty} d\tilde{q}_{\mu'} f(\tilde{q}_{\mu'}|\mu = \mu') \ . \tag{6.7}$$

The background only confidence level, CL_b, is the confidence level of an observation for a

hypothesis with $\mu = \mu'$ and the true value is $\mu = 0$ and is defined as [60]

$$\mathrm{CL}_b = p_b = \int_{\tilde{q}_{\mathrm{obs}}}^{\infty} d\tilde{q}_{\mu'} f(\tilde{q}_{\mu'}|\mu = 0)) \ . \tag{6.8}$$

Finally, CL_s is defined as the ratio of CL_{s+b} and CL_b, [60]

$$\mathrm{CL}_s(\mu) \equiv \frac{\mathrm{CL}_{s+b}}{\mathrm{CL}_b} \ . \tag{6.9}$$

This ratio effectively normalizes over the background leaving a metric that acts like a confidence level for just the signal. It is important to note that the CL_s is not a true confidence level and cannot be used for true Bayesian or frequentist statements [60]. The CL_s method is conservative, which means that a quoted CL_s value of 95% may actually have coverage greater than 95% but not less [61]. The associated frequentist-like statement is "95% of repeated experiments will exclude the signal hypothesis".

Figure 6.1 shows three plots: a curve of CL_s values calculated for each value of μ in the scan using 10000 of signal plus background toy events and 10000 background only toy events, as well as two curves showing the p_{s+b} and p_b values used in the CL_s calculation, Eq. (6.9). The curves for the CL_s and p_{s+b} are similar due to p_b approaching a constant. Shown in Figure 6.2 is data at the value of μ for which the $\mathrm{CL}_s \leq 0.05$ is obtained. The orange curve represents $f(\tilde{q}_{\mu'}|\mu = \mu')$, the test statistic under signal plus background data [59]. The filled orange is the p-value for signal plus background, $p_{\mu'}$. The blue curve represents $f(\tilde{q}_{\mu'}|\mu = 0)$ the test statistic under background only data. The filled blue is the p-value for background only, p_b [59]. The CL_s is essentially the filled orange normalized by the filled blue.

Upper Limits

Discovery of a signal is declared if the background only hypothesis is excluded. High energy physics (HEP) uses $5\,\sigma$ traditionally [59]. Exclusion of a signal hypothesis is declared if the signal plus background hypothesis has a small p-value. If $\mathrm{CL}_{s+b} < 0.05$, then we say the signal is excluded at 95% confidence [56]. If signal and background only hypotheses are similar, the CL_s method is implemented [62].

If neither the null, or signal hypothesis is sufficiently excluded by the data, we can instead construct an upper limit. This involves artificially increasing the signal strength until the desired confidence level is achieved. To set an upper limit, a "μ scan" is performed: CL_s is calculated for a range of μ values. When $\mathrm{CL}_s < 0.05$ for some value of $\mu = \mu_{0.05}$, we say that values of $\mu \geq \mu_{0.05}$ (signals that strong or stronger) are excluded at 95% confidence level

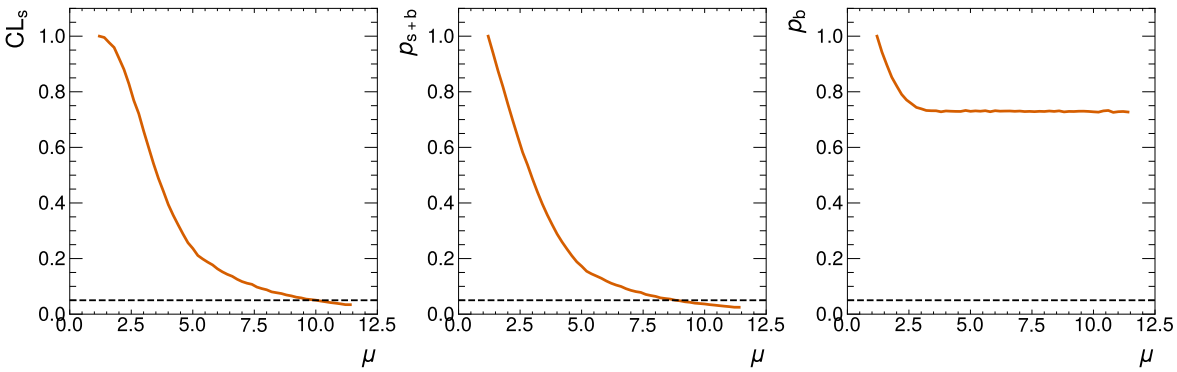

Figure 6.1: The first plot shows the CL_s calculated with toys for signal strength μ. The y-axis represents the CL_s and the x-axis represents μ. The dashed line at $y = 0.05$ represents the threshold for a 95% CL_s; it is achieved at $\mu = 10.1$. The second and third plots show the p-values for the signal plus background and background only hypotheses respectively. The CL_s is the ratio of p_{s+b} and p_b.

based on the observed data.

6.2 Implemented Statistical Analysis

The goal of this thesis was to use reported EWK W^+W^-jj cross-section predictions and measurements plus simulated, predicted SUSY cross-sections to calculate CL_s exclusions for the SUSY hypotheses. This is equivalent to a single bin histogram which contains a cross-section (rate) measurement. Unlike a counting experiment which uses the discrete Poisson distribution, this requires a continuous Gaussian. The cross-section can be multiplied by the luminosity to convert back to discrete events. The parameter of interest (POI) is the SUSY signal strength. In addition to the signal strength parameter, three nuisance parameters were included to take into account the reported systematic uncertainties of the theoretical background and signal predictions, and the measured observation.

For a given data measurement, d, the likelihood equation is the product of PDFs to represent the data and to constrain the nuisance parameters [6]

$$\mathcal{L}(\text{data}|\mu,\theta) = \text{Gaussian}(\text{data}|\mu \cdot s(\theta) + b(\theta)) \cdot p(\tilde{\theta}|\theta) \ . \tag{6.10}$$

The nuisance parameter constraint PDFs are Gaussian distributions centered at zero with width corresponding to their uncertainty

$$\frac{1}{\sqrt{2\pi}\sigma} e^{-\left(\frac{\theta}{\sqrt{2}\sigma}\right)^2} \ . \tag{6.11}$$

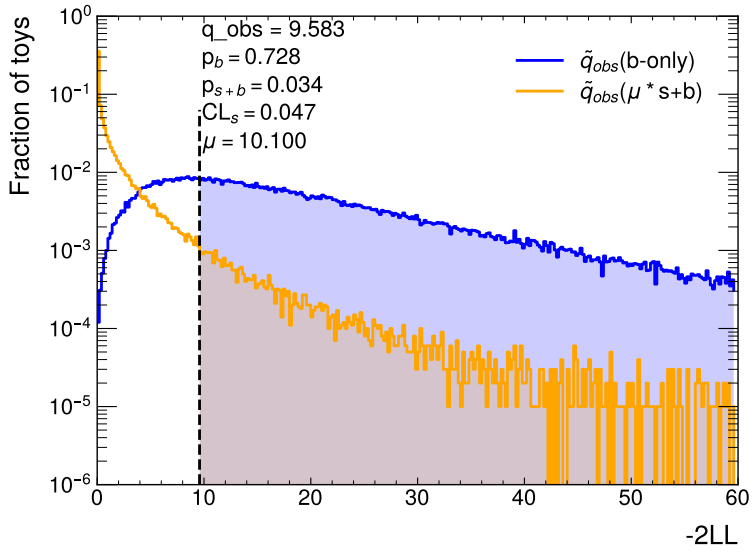

Figure 6.2: The distribution of the test statistic $\tilde{q}_{\text{obs}}$ calculated on 10000 toys for the background only hypothesis (blue) and signal plus background hypothesis for signal strength μ (orange). The y-axis represents the fraction of toys and the x-axis represents twice the negative log likelihood value. The μ value for 95% CL_s is shown with a dashed vertical line at $x = 10.1$. The corresponding values are noted: $\tilde{q}_{\text{obs}} = 0.583$, $p_s = 0.728$, $p_{s+b} = 0.034$, CL_s =0.047. The shaded region indicates the area integrated to calculate the p-values.

In this thesis, the Gaussian approximation of a Poisson is used as the data PDF

$$\mathcal{L}(\mu) = \frac{1}{\sqrt{2\pi}\sigma_{d,stat}} e^{-\left(\frac{\mu(s_0+\delta s_0)+b+\delta b-d+\delta_d}{\sqrt{2}\sigma_{d,stat}}\right)^2} \times \frac{1}{\sqrt{2\pi}\sigma_{d,sys}} e^{-\left(\frac{\delta d}{\sqrt{2}\sigma_{d,sys}}\right)^2} \times \frac{1}{\sqrt{2\pi}\sigma_{s_0}} e^{-\left(\frac{\delta s_0}{\sqrt{2}\sigma_{s_0}}\right)^2} \times \frac{1}{\sqrt{2\pi}\sigma_b} e^{-\left(\frac{\delta b}{\sqrt{2}\sigma_b}\right)^2} \quad (6.12)$$

. Here μ is the POI signal strength parameter, σ_{s_0} and σ_b are the signal uncertainty and reported background uncertainty. The variable b is the background ($\mu = 0$) and s_0 is the nominal ($\mu = 1$) signal prediction. The parameters δb and δs allow the background and signal to float within their uncertainties, they are constrained to a Gaussian centered at zero with standard deviation equal to the uncertainty.

The uncertainty associated with a counting experiment (Poisson) is a statistical uncertainty, $\sqrt{N}$. Systematic and statistical uncertainties add in quadrature $\sigma^2_{sys}+\sigma^2_{stat} = \sigma^2_{total}$ [5]. The reported uncertainty represents σ_{total}, statistical uncertainty accounted for in the Poisson can be subtracted out and the remainder assigned to σ_{sys} [5]. The uncertainty σ_{sys} is

then used in the Gaussian constraint term for the data nuisance parameter.

To compare compatibility of the data to the null (i.e. background only) and signal plus background hypotheses, the test statistic $\tilde{q}_\mu$ is used [59]

$$\tilde{q}_\mu = -2 \ln \frac{\mathcal{L}(\text{data}|\mu, \hat{\theta}_\mu)}{\mathcal{L}(\text{data}|\hat{\mu}, \hat{\theta})}, \ 0 \leq \hat{\mu} \leq \mu \ . \tag{6.13}$$

It is based on the profile likelihood ratio. The "data" can be the actual measurement or pseudo-data toys generated to construct sampling distributions. The θ represents all nuisance parameters. The signal strength is μ. The lower constraint is to ensure positive signal [59]. The upper constraint dictates a one-sided confidence interval; it deems upward fluctuations in data such that $\hat{\mu} > \mu$ to not be evidence against a signal hypothesis μ. If we see more that what we expect from a signal hypothesis, that should not rule out that hypothesis.

In order to calculate CL_s, the following distributions are needed: $f(\tilde{q}_\mu|\mu = 0))$ and $f(\tilde{q}_\mu|\mu = \mu'))$ [59]. There are two different approaches. One way is to apply asymptotic approximations which are computationally cheap but rely on certain conditions for accurate results. The second method is to generate pseudo-data experiments to manually sample the distribution. It is computationally expensive but it will work for cases not suitable for asymptotics.

6.2.1 Asymptotic Approximation Method

In the large sample limit, the test statistic distributions can be approximated using Wilks' and Wald's theorems [59]. Wilks' theorem is the asymptotic approximation. Let the profile likelihood ratio $\lambda(x;\mu)$ be the test statistic for one POI, μ. Wilks' theorem states that in the large sample limit, $Q = -2 \ln \lambda(x;\mu)$ will approach a χ^2 distribution if the μ hypothesis is correct. Wilks' also applies if there are n nuisance parameters θ, and the profile likelihood ratio is defined by [59]

$$\lambda(\mu) = \frac{\mathcal{L}(x;\mu,\hat{\hat{\theta}}_\mu)}{\mathcal{L}(x;\hat{\mu},\hat{\theta})}. \tag{6.14}$$

Wilks' theorem will not hold if there are bounds on the nuisance parameters.

The test statistic, Q, calculated for a hypothesis of $\mu = \mu'$ for data distributed according to a $\mu = \mu'$ hypothesis, will follow a χ^2 distribution. If however, the data is actually distributed according to some other $\mu_{\text{data}} \neq \mu'$, the test statistic will follow a non-central χ^2

with non-centrality parameter Λ

$$Q = -2\ln\lambda(\mu) = \frac{(\mu-\hat{\mu})^2}{\sigma^2} + \mathcal{O}(1/\sqrt{N}) \tag{6.15}$$

where $\hat{\mu}$ is a Gaussian distributed variable with central value μ' and scale σ, and N is the number of data points in sample [59]. For $N >> 1$, the distribution can be approximated by

$$f(t_\mu|\Lambda) = \frac{1}{2\sqrt{t_\mu 2\pi}}\left[\exp\left(-\frac{1}{2}\left(\sqrt{t_\mu}+\sqrt{\Lambda}\right)^2\right) + \exp\left(-\frac{1}{2}\left(\sqrt{t_\mu}-\sqrt{\Lambda}\right)^2\right)\right] \tag{6.16}$$

where the non centrality parameter Λ is defined as [59]

$$\Lambda = \frac{(\mu-\mu')^2}{\sigma^2}\ . \tag{6.17}$$

If indeed $\mu = \mu'$, $\Lambda = 0$, and the standard χ^2 distribution is recovered. An artificial data set called "Asimov data" can be used to estimate Λ [59]. The Asimov data set represents the median dataset for a hypothesis. It is defined so that estimators evaluated on the Asimov data will return the true parameters. For a single bin it is simply the expected value; $A_b = b$ for the background only hypothesis and $A_{s+b} = \mu s + b$ for some alternate signal hypothesis [59]. From the Asimov data, the Asimov likelihood $\mathcal{L}_A$ and the likelihood ratio λ_A can be calculated

$$\lambda_A(\mu) = \frac{\mathcal{L}_A(\mu,\hat{\hat{\theta}})}{\mathcal{L}_A(\hat{\mu},\hat{\theta})} = \frac{\mathcal{L}_A(\mu,\hat{\hat{\theta}})}{\mathcal{L}_A(\mu',\theta')} \tag{6.18}$$

due to the fact that $\hat{\mu} = \mu'$ and $\hat{\theta} = \theta'$ for the Asimov data, by construction [59]. Due to the result from Wilks and Wald [59]

$$q_{\mu,A} = -2\ln\lambda_A(\mu) \approx \frac{(\mu-\mu')^2}{\sigma^2} = \Lambda\ . \tag{6.19}$$

The variance of $\hat{\mu}$ can therefore be approximated with

$$\sigma_A^2 = \frac{(\mu-\mu')^2}{q_{\mu,A}} \tag{6.20}$$

where $q_{\mu,A}$ is the test statistic calculated for a hypothesis μ on the Asimov data set [59]. When setting the exclusion limits of the signal hypothesis, one assumes that there is no

signal in the data (background only), so $\mu' = 0$. The variance equation simplifies to [59]

$$\sigma_A^2 = \frac{\mu^2}{q_{\mu,A}} \ . \tag{6.21}$$

For discovery of a signal, the null hypothesis must be rejected with a confidence level of 95%. The null hypothesis of $\mu = 0$ is tested against the data assumed to have a signal strength μ'.

A subtlety comes up when performing a μ scan for setting CL_s limits. As mentioned before, CL_s is the ratio of p-values for a hypothesis μ calculated as if the signal plus background hypothesis ($\mu = \mu' \neq 0$) is true and for if the background only hypothesis ($\mu' = 0$) is true. First, the observed data is used to calculate the test statistic, q, for the μ hypothesis, $q_{\mathrm{obs},\mu}$. Eq. (6.21) can directly be used to calculate σ_b which can then be used in the approximation to find $f(q_\mu|0)$ and p_b. However, Eq. (6.20) cannot be directly used to get σ_{s+b} since by definition $\Lambda = 0$ if $\mu = \mu'$. Recall in Eq. (6.19), σ^2 is dependent on μ' but not μ. This is because σ^2 is the variance of $\hat{\mu}$, which has mean μ', and is generally unrelated to μ. Eq. (6.19) is just a method of approximation which happens to use μ. If a stand in for μ is used that is sufficiently large to avoid the discontinuity, Eq. (6.19) can be used to find σ_{s+b}, $f(q_\mu|\mu')$, and p_{s+b}.

These approximations can greatly save computing time provided they are valid. Unfortunately, these approximations only hold as long as Wilks and Wald's theorem hold. Generally, they hold for Poissonian likelihoods with large event counts since for Poisson likelihoods, the relative uncertainty is proportional to $1/\sqrt{N_{\mathrm{events}}}$. It fails for low numbers of events because the relative uncertainty is too great. In the case of this thesis, the relative uncertainty of the observation is 20% and this renders the χ^2 approximation invalid. Figure 6.3a shows how the toy data that does not account for the systematic uncertainty does not agree with the χ^2 approximation which is the required assumptions needed for Wilks' theorem. The large uncertainty on the observation leads to poor resolving power; an added signal can be easily absorbed by the data uncertainties. Since smaller values of a test statistic represent better agreement between observation and hypothesis, this leads to smaller test statistic values than predicted by the asymptotic approximations. Figure 6.3b shows how the toy data that does account for the large data systematic uncertainty in the likelihood does not follow the χ^2 approximation either. Figure 6.3c shows that this leads to the upper limits being overestimated with the asymptotic approximation compared to the limit calculated with toys without the data uncertainty information but underestimated when compared to the limit calculated with toys with the data uncertainty information included.

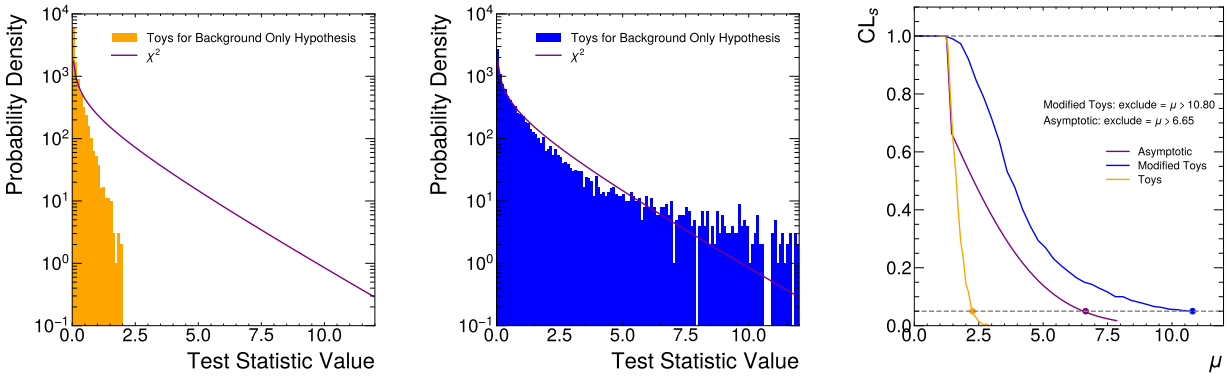

(a) (b) (c)

Figure 6.3: Comparison of the asymptotic approximation versus toys for setting limits with the likelihood Eq. (6.12). The plot of probability versus test statistic in (a) shows the asymptotic approach is invalid for this analysis because the orange test statistic drawn from toys based on the likelihood without accounting for the large systematic uncertainty of the data does does not follow the purple χ^2 distribution. The similar comparison in plot (b) shows the toys drawn from a likelihood that does account for the large data systematic uncertainty does not follow the purple χ^2. The plot of CL_s vs μ shown in (c) depicts observed CL_s limits calculated using asymptotic approximation (purple), toys without data uncertainty (orange) and toys with data uncertainty (blue). The dashed line at $y = 0.05$ represents the threshold for a 95% CL_s.

6.2.2 Pseudo-Data Toy Method

An alternative to the asymptotic approximation approach is to realize the data distribution by generating pseudo-data toys for a desired signal strength μ'. The test statistic is then calculated for each toy. The set of test statistics represents a sampling of $f(q_\mu|\mu')$.

The goal is to utilize measurements performed from two different experiments, CMS and ATLAS, to make statements on the same hypothesis. This has been done before, notably for the analyses leading up to the Higgs boson discovery in 2012 [60]. A method was derived that allows pseudo-data toys involving nuisance parameters to be generated in a pure frequentist manner [60]. This is the basis for the method taken in this thesis. It is important to note that as with much of statistics, there is not one universally correct approach. Factors such as convention, convenience, and what information is available, lead to an appropriate method. The important part is to stay consistent and be clear on what conclusions can be drawn from the analysis results.

In a classical frequentist approach for discrete events with no nuisance parameters, pseudo-data toys are drawn from a simple Poisson distribution for some rate correspond-

ing to either signal plus background or background only [5]. Introducing nuisance parameters complicates matters in a few ways by adding new degrees of freedom. Care must be taken to avoid double-counting the extra freedom between generating pseudo-data and fitting the data in the likelihood. The choice made in [60, 63] is to calculate the nuisance parameters' best fit values for the observed (real) data under the appropriate signal strength hypothesis, $\hat{\theta}_{\mu}^{\text{obs}}$.This is done by maximizing the likelihood over the nuisance parameters, θ, while keeping the signal strength, μ, fixed. Practically, this is done by minimizing twice the negative log likelihood. The toys can then be drawn from a Poisson with a fixed rate $\nu = \mu \cdot s(\hat{\theta}_{\mu}^{\text{obs}}) + b(\hat{\theta}_{\mu}^{\text{obs}})$. When the toys are processed through the likelihood to calculate the test statistic, the nuisance parameters are once again allowed to float in any required fits. To summarize, toys are generated for a given hypotheses from a Poisson with a fixed rate motivated by the hypothesis and the real observed data. The toys are then processed and treated as real data.

The chosen test statistic is

$$\tilde{q}_{\mu} = -2 \ln \frac{\mathcal{L}(\text{data}|\mu, \hat{\theta}_{\mu})}{\mathcal{L}(\text{data}|\hat{\mu}, \hat{\theta})}, \ 0 \leq \hat{\mu} \leq \mu \tag{6.22}$$

To construct the CL_s limits, different sets of pseudo-data representing the null hypothesis and every signal strength hypothesis in the μ scan are needed. The parameters $\hat{\theta}_0^{\text{obs}}$ and $\hat{\theta}_{\mu}^{\text{obs}}$ are the best fit values for the nuisance parameters for the observed data under the background-only and signal+background hypotheses. These are found by maximizing the likelihood for fixed $\mu = 0$ or $\mu = \mu'$ respectively. The pseudo-data is constructed by fixing $\hat{\theta}_0^{\text{obs}}$ or $\hat{\theta}_{\mu}^{\text{obs}}$ and drawing from a Poisson for $\mu = \mu, \hat{\theta}_{\mu}^{\text{obs}}$ and $\mu = 0, \hat{\theta}_0^{\text{obs}}$. The test statistic is calculated on the two pseudo-data sets to make the PDFs $f(\tilde{q}_{\mu}|\mu, \hat{\theta}_{\mu}^{\text{obs}})$ and $f(\tilde{q}_{\mu}|\mu = 0, \hat{\theta}_0^{\text{obs}})$. When calculating the test statistics, $\hat{\theta}_0^{\text{obs}}$ and $\hat{\theta}_{\mu}^{\text{obs}}$ are allowed to float in the required fits; they are only fixed when generating the pseudo-data. The systematic uncertainties (nuisance parameters) are assumed to be completely uncorrelated.

Systematic errors have a PDF $\rho(\theta|\tilde{\theta})$ [60]. In the framework of Bayesian statistics, this can be interpreted as the posterior probability for some measurements (real or imaginary) $\tilde{\theta}$ and a "prior" $\pi_{\theta}(\theta)$

$$\rho(\theta|\tilde{\theta}) \sim p(\tilde{\theta}|\theta) \cdot \pi_{\theta}(\theta) \ . \tag{6.23}$$

The distribution $p(\tilde{\theta}|\theta)$ can be considered a frequentist likelihood [60]. The PDF $p(\tilde{\theta}|\theta)$ is then used in the frequentist sense as a constraint term for the nuisance parameters in the full likelihood; they can float in the fits but are penalized for straying far from the nominal

	Bayesian Probability Distribution	Frequentist Likelihood	Prior Probability
	$\rho(\theta\|\tilde{\theta})$	$p(\tilde{\theta}\|\theta)$	$\pi_\theta(\theta)$
Gaussian	$\frac{1}{\sqrt{2\pi}\sigma}\exp\left(-\frac{(\theta-\tilde{\theta})^2}{2\sigma^2}\right)$	$\frac{1}{\sqrt{2\pi}\sigma}\exp\left(-\frac{(\tilde{\theta}-\theta)^2}{2\sigma^2}\right)$	flat

Table 6.1: Comparison of Bayesian and frequentist interpretations of nuisance parameter distributions [60].

values. The PDF $p(\tilde{\theta}|\theta)$ can also be used in the sampling distributions for the test statistic.

If the Bayesian posterior $\rho(\theta|\tilde{\theta})$ is modeled with a Gaussian centered at $\tilde{\theta}$, and the prior probability $\pi_\theta(\theta)$ is flat, then the frequentist likelihood $p(\tilde{\theta}|\theta)$ is also a Gaussian centered at $\tilde{\theta}$. But whereas $\rho(\theta|\tilde{\theta})$ is conceptually a function of θ for fixed $\tilde{\theta}$; $p(\tilde{\theta}|\theta)$ is conceptually a function of $\tilde{\theta}$ for fixed θ. Practically, because we are using Gaussians that are symmetric, they are identical Gaussians. This comparison is shown in Table 6.1. For this thesis, the background, signal, and data nuisance parameters have $\tilde{\theta} = 0$. Adding nuisance parameters reduces the sensitivity of a search as it allows a hypothesis to absorb data fluctuations that a more rigid test might deem as signal [60]. However, they can also tighten the observed limits if the nuisance parameters float in a way that bolsters the background prediction, allowing smaller signals to be ruled out.

6.2.3 Toy Model Data

The values used in the creation of the example plots are shown in Table 6.2.

	Cross-section [pb]	Events
Signal	0.711	99.5
Background	9.1	1274
Observed data	10.2	1428
σ_s	0.05	7
σ_b	0.6	84
σ_d	2	280

Table 6.2: The values used in shown example plots. σ_s, σ_b, σ_d are the uncertainties for the signal, background, and observed data. The number of events is calculated by multiplying the cross-section by a luminosity of $140\,\text{fb}^{-1}$.

6.2.4 Modified Likelihood and Toy Generation

Though the above approach was taken from a trusted source, the case considered did not have an uncertainty on the observed measurement like the case in this thesis does. When treated like the other nuisance parameters, the uncertainty on the data led to upper limits much tighter than expected. With the example numbers $\mu \approx 5$ is expected to be excluded but the toys gave an upper limit of $\mu = 2.26$. That is well within the data uncertainty and should not be excluded.

Considering the simple Poisson case, toys are drawn from a Poisson which includes a statistical uncertainty. They are then run through a likelihood which is again based on a Poisson and so includes a statistical uncertainty. In this case, while there is the statistical component to uncertainty, there is also a systematic uncertainty due to the unfolding of the measurement. Rather than pull from a statistical Gaussian (equivalent to a Poisson in limit of large N) then smear that toy with a systematics Gaussian, toys can be pulled from a Gaussian with the total data uncertainty. The toys are drawn from a Gaussian centered at $\hat{\nu} = \mu \cdot s(\hat{\theta}_\mu^{\text{obs}}) + b(\hat{\theta}_\mu^{\text{obs}})$, where $\hat{\theta}_\mu^{\text{obs}}$ is the nuisance parameter's best fit value for the observed data under the appropriate signal strength hypothesis. The Gaussian has width $\frac{\sigma_d}{d} \times \hat{\nu}$, which is the relative total observed data uncertainty converted to an absolute uncertainty for $\hat{\nu}$. Each toy is given an uncertainty $\sigma_{total} = \frac{\sigma_d}{d} \times$ toy.

In the likelihood, the statistical uncertainty is based on the rate predicted by the hypothesis ($\sigma_{stat} = \sqrt{\nu}$) and it is included as the main body of the likelihood. The statistical uncertainty is subtracted from the total in quadrature, $\sigma_{sys} = \sqrt{\sigma_{total}^2 - \sigma_{stat}^2}$. The remaining systematic uncertainty is treated as a nuisance parameter to constrain δ_d. The modified likelihood is

$$\mathcal{L}(\mu) = \frac{1}{\sqrt{2\pi}\sigma_{d,stat}} e^{-\left(\frac{\mu(s_0+\delta s_0)+b+\delta b-d+\delta_d}{\sqrt{2}\sigma_{d,stat}}\right)^2} \times \frac{1}{\sqrt{2\pi}\sigma_{d,sys}} e^{-\left(\frac{\delta d}{\sqrt{2}\sigma_{d,sys}}\right)^2} \times \frac{1}{\sqrt{2\pi}\sigma_{s_0}} e^{-\left(\frac{\delta s_0}{\sqrt{2}\sigma s_0}\right)^2} \times \frac{1}{\sqrt{2\pi}\sigma_b} e^{-\left(\frac{\delta b}{\sqrt{2}\sigma_b}\right)^2} . \quad (6.24)$$

The modified upper limit is found to be $\mu_{0.05} = 10.8$. This approach gives upper limits that are consistent with the expectations that adding the data uncertainty leads to weaker bounds. The value itself is consistent with a naive estimate of $\mu_{0.05} = 5$.

Unfortunately the results with the modified toys are still incompatible with the asymptotic approximations. The toys lead to weaker bounds than the approximation which is acceptable since toys account for the large data uncertainty. The asymptotic approximation

underestimates the test statistic distribution when there is a large data uncertainty.

Chapter 7

Results

After simulating the SUSY signal samples, the selection criteria for EWK W^+W^-jj is applied to see how many SUSY events would be present in the fiducial signal regions. This is done for each of the SUSY mass points for both the CMS and ATLAS signal regions. The systematic and statistical uncertainties are calculated for the SUSY events passing the selection criteria. Systematic uncertainties include the scale uncertainties, PDF uncertainties, and `xqcut` uncertainties, as outlined in Section. 5.4. Upper CL_s limits are computed for the potential presence of SUSY signals using the modified toy method outlined in Section 6.2.4.

7.1 Simulated SUSY Cross-Sections in VBS Phase Space

The mass difference between the chargino and the neutralino, ΔM, dictates the final states. For example, if $\Delta M < M_W$ then the charginos cannot decay to on-shell W bosons. Figure 7.1 plots the signal cross-section of all the SUSY mass points against ΔM. CMS and ATLAS signal regions are differentiated by the marker shape. Mass points in a group such as fixed $M_{\chi^\pm}$, M_{χ^0}, or along the boundary curve are indicated by colour that corresponds to those in Figure 3.4. For fixed chargino mass, larger ΔM is associated with larger cross-sections since it is achieved with a lighter neutralino. For fixed neutralino mass, the cross-sections decrease with larger ΔM, as it means the chargino mass increases and heavier charginos are produced less frequently.

The cross-sections in the ATLAS signal region display the same trends but are approximately an order of magnitude smaller than for the CMS signal region. Recall, as shown in Table 5.3, CMS includes the same flavour lepton channels which increases the phase space which in turn encompasses more SUSY events. Figure 7.3 shows the SUSY cross-sections relative to the respective SM EWK W^+W^-jj cross-section to better compare sensitivity to BSM physics between ATLAS and CMS. The CMS criteria leads to larger SUSY cross-

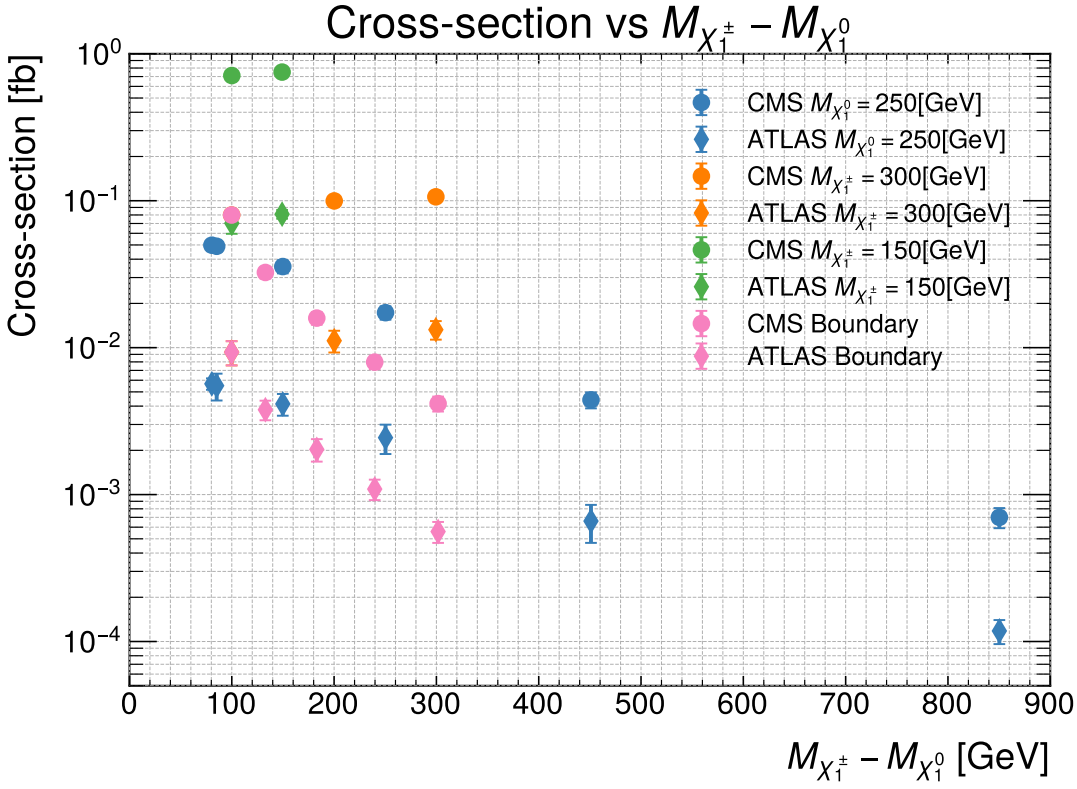

Figure 7.1: The y-axis represents the SUSY signal cross-section passing EWK W^+W^-jj phase space criteria for each SUSY mass point and the x-axis represents the mass difference between the chargino and lightest neutralino. The diamonds represent the ATLAS criteria and the circles represent CMS. The colors correspond to the sets of masses from Figure 3.4. The range of cross-section magnitude for mass differences between $100 - 200$GeV shows that the mass difference is not the only factor affecting SUSY production cross-sections; the mass of the chargino is also important.

sections relative to the SM signal than the ATLAS criteria. This is potentially due to the attributes of the CMS selection criteria that are looser compared to the selection criteria used by ATLAS being better aligned with the SUSY event characteristics. Attributes that differ between ATLAS and CMS include allowed lepton flavor combinations, number of leptons, and jet or lepton invariant mass, as shown in Table 5.3.

The on-shell cross-sections fall exponentially, so plotting with a log scaled y-axis gives a negative, linear slope. Table 7.1 shows the cross-section for each of the SUSY signal mass points in ATLAS and CMS EWK W^+W^-jj signal regions. The rounding conventions from the PDG [6] were used.

$M_{\chi_1^\pm}$ [GeV]	$M_{\chi_1^0}$ [GeV]	σ_{ATLAS} [fb]	σ_{CMS} [fb]
330	250	0.0057 ± 0.0005	0.050 ± 0.004
335	250	0.0055 ± 0.0011	0.049 ± 0.004
400	250	0.0041 ± 0.0007	0.036 ± 0.004
500	250	0.0024 ± 0.0006	0.0173 ± 0.0018
700	250	0.00066 ± 0.00019	0.0044 ± 0.0005
1100	250	0.000118 ± 0.000022	0.00070 ± 0.00011
300	1	0.0133 ± 0.0019	0.106 ± 0.008
300	100	0.0112 ± 0.0019	0.100 ± 0.008
300	200	0.0093 ± 0.0017	0.080 ± 0.007
150	1	0.081 ± 0.006	0.75 ± 0.05
150	50	0.070 ± 0.011	0.71 ± 0.05
300	200	0.0093 ± 0.0017	0.080 ± 0.007
400	268	0.0038 ± 0.0006	0.0325 ± 0.0029
500	317	0.00203 ± 0.00035	0.0159 ± 0.0016
600	360	0.00109 ± 0.00017	0.0080 ± 0.0008
700	400	0.00056 ± 0.00009	0.0042 ± 0.0005

Table 7.1: The passing cross-sections for various chargino and neutralino masses in the ATLAS [9] and CMS [10] signal regions. The signal events were simulated with MADGRAPH and PYTHIA. The uncertainties are the total of the statistical and systematic (scale and PDF) uncertainties calculated with MADGRAPH.

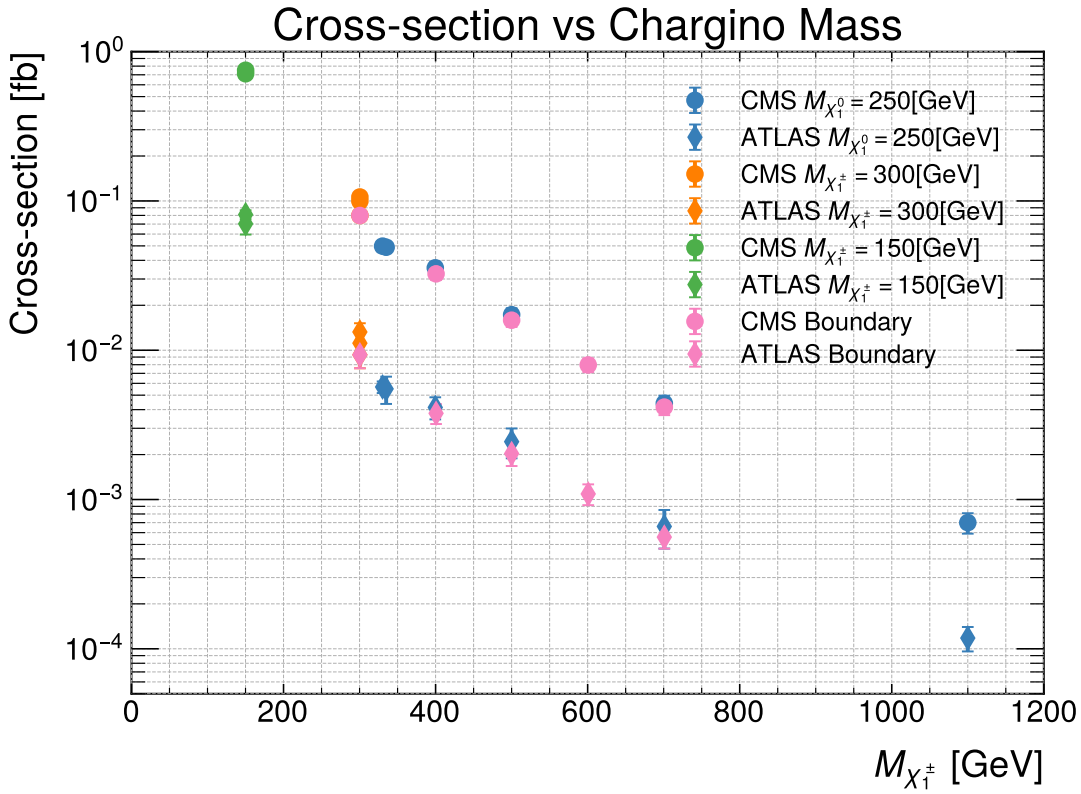

Figure 7.2: The y-axis represents the SUSY signal cross-section passing EWK W^+W^-jj phase space criteria for each SUSY mass point and the x-axis represents the chargino mass. The diamonds represent the ATLAS criteria and the circles represent CMS. The colors correspond to the sets of masses from Figure 3.4. Points in vertical lines correspond to fixed chargino mass and different neutralino masses. The cross-section decreases with increased chargino mass. The CMS selection criteria accepts more SUSY events than the ATLAS criteria. Increasing $M_{\chi^\pm}$ corresponds to decreasing cross-section.

7.2 Upper Limits of BSM Signal

The upper limits are calculated using the CL$_s$ method introduced in Section 6.1.2 with pseudo-data toys as described in Section 6.2.4 [60]. The upper limit is calculated for the SUSY mass point that results in the largest potential signal cross-section for both the CMS and ATLAS signal regions, ($M_{\chi^\pm} = 150\,\text{GeV}$, $M_{\chi^0} = 50\,\text{GeV}$). Though this mass point has been excluded by experiment, it provides insight on the highest level of sensitivity possible to expect [37].

There are light SUSY mass points not yet excluded by experiment such as ($M_{\chi^\pm} = 330\,\text{GeV}$, $M_{\chi^0} = 250\,\text{GeV}$) [37, 42]. The upper limit is also calculated for the SUSY point

Mass Point ($M_{\chi^{\pm}}[GeV]$, M_{χ^0}[GeV])	ATLAS (μ_{upper})	CMS (μ_{upper})
$(150, 1)$	24	10
$(150, 1)$ Higher precision	16	6
$(330, 250)$	360	150
$(330, 250)$ Higher precision	220	91

Table 7.2: Upper CL_s limits of the SUSY signal strength present in EWK W^+W^-jj phase-space, μ, is calculated for the $(150, 1)$ and $(330, 250)$ mass points for ATLAS and CMS. The current published EWK W^+W^-jj measurement uncertainty is used. The hypothetical higher precision based on the current $W^{\pm}W^{\pm}jj$ measurement uncertainty is used as a comparison.

with the largest cross-section that has yet to be excluded by experiment, ($M_{\chi^{\pm}} = 330\,\text{GeV}$, $M_{\chi^0} = 250\,\text{GeV}$). This is done both to compare the sensitivity to that of the benchmark set by the already excluded point and to observe the strength of a potential new limit.

Currently, the uncertainty for the CMS SM EWK W^+W^-jj measurement is approximately 40 times larger than this potential SUSY contribution, while the ATLAS uncertainty is approximately 88 times larger. For comparison, the SUSY contribution to the cross-section for the mass point ($M_{\chi^{\pm}} = 150\,\text{GeV}$, $M_{\chi^0} = 1\,\text{GeV}$) is approximately three times smaller than the CMS SM EWK W^+W^-jj measurement uncertainty or approximately six times smaller than the ATLAS measurement uncertainty. Same sign WW in association with two jets ($W^{\pm}W^{\pm}jj$) is another VBS process that has been measured by CMS and ATLAS [13, 14]. Notably, $W^{\pm}W^{\pm}jj$ does not have to contend with Drell-Yan or $t\bar{t}$ background and so it can allow same flavour lepton pairs in the signal region without the need for stronger kinematic cuts [23]. There are also no gluon initiated diagrams. This leads to smaller uncertainties on the measurements for $W^{\pm}W^{\pm}jj$ compared to EWK W^+W^-jj.

CMS measured the $W^{\pm}W^{\pm}jj$ cross-section to be 3.98 ± 0.45 ($0.37\,(\text{stat.}) \pm 0.25\,(\text{syst.})$) fb; a total relative uncertainty of 11.3% [14]. Comparatively, CMS EWK W^+W^-jj has a relative uncertainty of 19.8%. ATLAS measured the $W^{\pm}W^{\pm}jj$ cross-section to be $2.92 \pm 0.22(\text{stat.}) \pm 0.19(\text{syst.})$ fb; the total uncertainty is 0.29 fb and the total relative uncertainty is 10% [13]. Comparatively, ATLAS EWK W^+W^-jj has a relative uncertainty of 18.5%. This comparison is shown simply to give a realistic expectation for potential precision improvement with the EWK W^+W^-jj measurement.

Assuming an integrated luminosity of $L = 140\,\text{fb}^{-1}$, and 100% efficiency, the expected number of events is given by $N = \sigma \times L$ [5]. The maximum number of SUSY events that would pass the EWK W^+W^-jj selection criteria at CMS is 105 ± 7 events. Comparatively,

the SM EWK W^+W^-jj measurement has an uncertainty of 280 events. If sensitivity was improved to the level of the easier to measure same sign $W^{\pm}W^{\pm}jj$, the uncertainty would be approximately 161 events. For the ATLAS search, the maximum number of SUSY events is 11.3 ± 0.8 events compared to the SM error of 70 events. If sensitivity was improved to the level of the easier to measure same-sign $W^{\pm}W^{\pm}jj$, the uncertainty would be approximately 38 events. Figure. 7.4 shows CL_s plots comparing the limits for the SUSY mass point with the largest cross section with the current uncertainty and with the fictionally reduced uncertainty. Additionally the CL_s for the SUSY mass point with the largest cross section that is not yet excluded by experiment is shown. The upper CL_s limits of the SUSY signal strength present in the EWK W^+W^-jj phase space, μ, are summarized in Table 7.2.

In both CMS and ATLAS VBS signal regions, even with nearly twice the precision, the SUSY signal would not be detectable. Chargino masses that have been previously excluded with other methods are not able to be excluded here. SUSY exclusion boundaries were not able to be extended for previously unexcluded chargino mass points.

Measurements of SM EWK W^+W^-jj can be made in confidence that the results are not contaminated by SUSY signals. Specifically, dichargino production modeled with a Bino-Wino simplified MSSM framework will not affect precision measurements of EWK W^+W^-jj. Though dichargino production was shown to mimic the signal of EWK W^+W^-jj, the selection criteria was not optimal. Searches for SUSY signals of this type could continue in difference phase spaces better suited to the dichargino event topology.

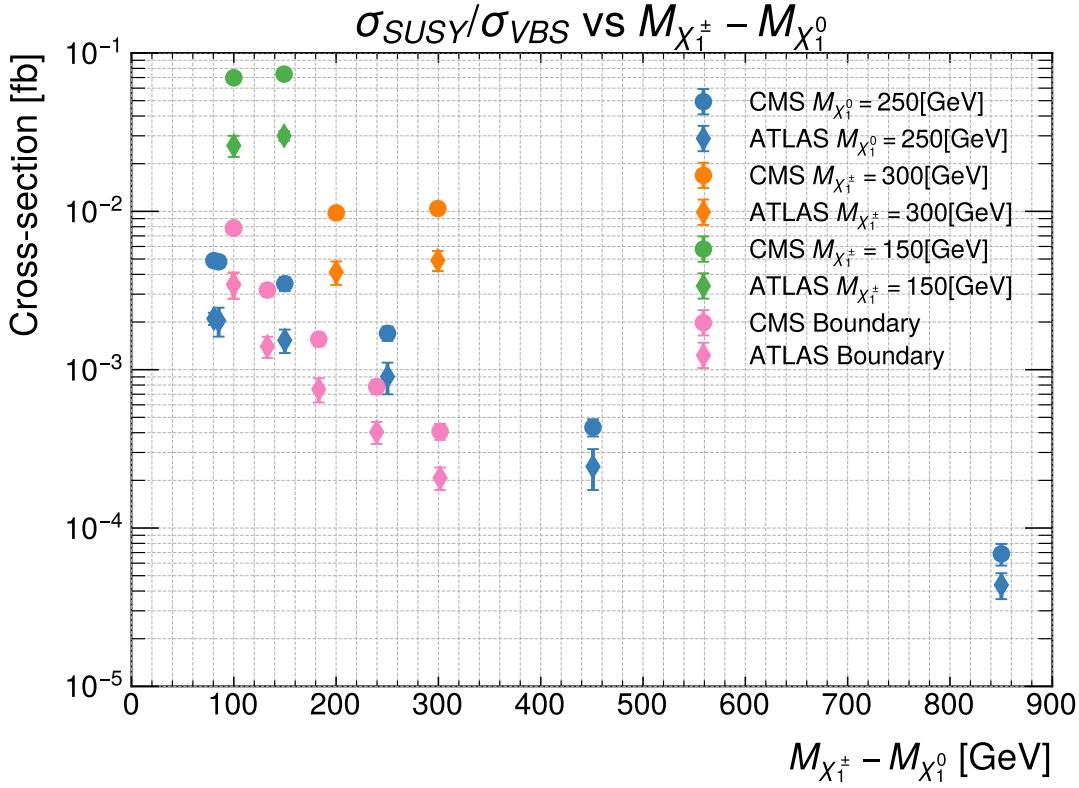

Figure 7.3: The y-axis represents the SUSY signal cross-section passing EWK W^+W^-jj phase space criteria divided by the respective SM cross-section measurement for each SUSY mass point. This is done to compare the fraction of signal region cross-section that could be SUSY. The x-axis represents the mass difference between the chargino and lightest neutralino. The diamonds represent the ATLAS criteria and the circles represent CMS. The colors correspond to the sets of masses from Figure 3.4. The cross-section magnitude trends are unchanged by the normalization; the CMS criteria results in a larger cross-section than the ATLAS criteria.

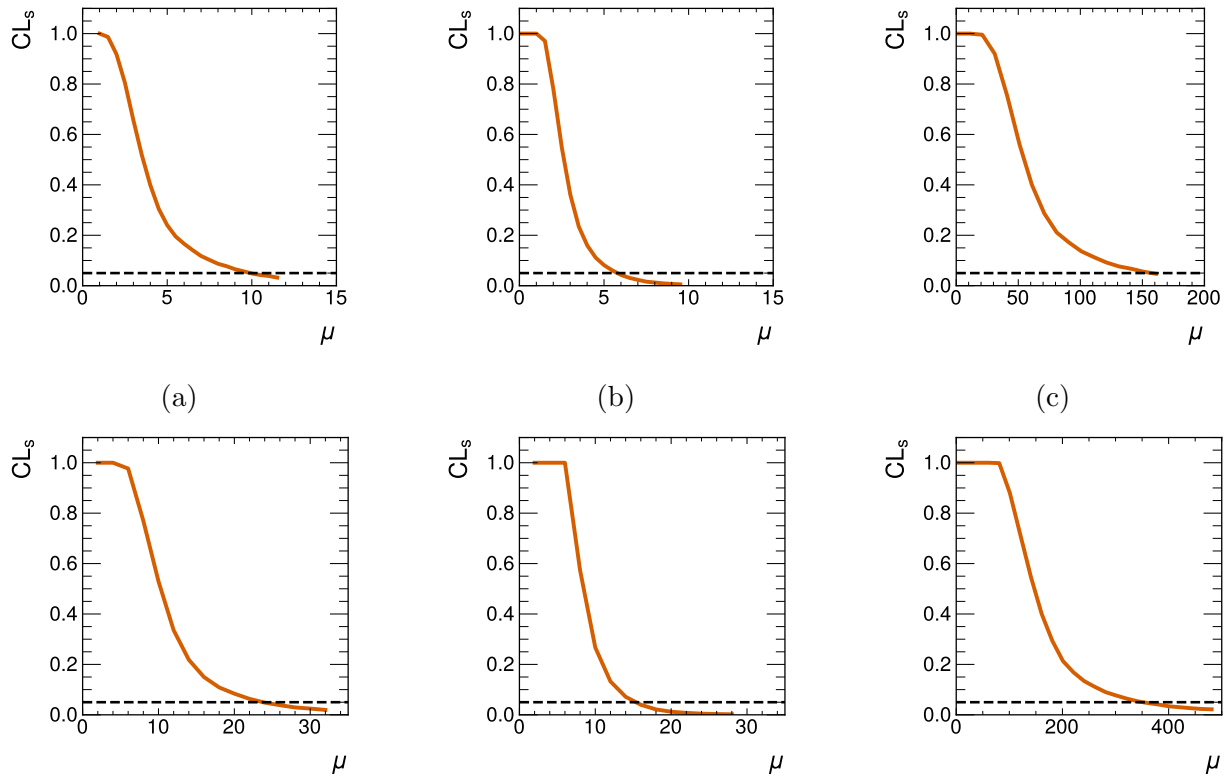

Figure 7.4: The CL$_s$ upper limits from the CMS data for mass point (a). ($M_{\chi^\pm}$=150 GeV, M_{χ^0}=1 GeV), (b). ($M_{\chi^\pm}$=150 GeV, M_{χ^0}=1 GeV) with 10% uncertainty, (c). ($M_{\chi^\pm}$=330 GeV, M_{χ^0}=250 GeV). From the ATLAS data for mass point (d). ($M_{\chi^\pm}$=150 GeV, M_{χ^0}=1 GeV), (e). $M_{\chi^\pm}$=150 GeV, M_{χ^0}=1 GeV) with 10% uncertainty, (f). ($M_{\chi^\pm}$=330 GeV, M_{χ^0}=250 GeV). An increase in the precision of the data measurement by a factor of two is not sufficient to resolve the SUSY signal.

Chapter 8

Conclusion

There is evidence from across physics specialties that there is physics beyond what is described by the current Standard Model. The electroweak scattering of two oppositely charged W bosons is a process that is sensitive to BSM physics. It is an important probe into the electroweak sector and EFT frameworks. It is a difficult measurement that results in a large uncertainty. Physics beyond the Standard Model could be present in the VBS phase space.

Supersymmetry is a BSM theory motivated by symmetries and the hierarchy problem. A simplified Bino-Wino version of the Minimal Supersymmetric Standard Model was utilized to examine the potential for BSM particle signals in SM VBS measurements. New particles, such as charginos and neutralinos, are predicted by the SUSY model. Charginos decay to SM W bosons and could therefore leave the same detector signature as EWK W^+W^-jj. The production of two charginos plus two jets was simulated with MADGRAPH, PYTHIA, and DELPHES for a range of potential chargino masses calculated with SOFTSUSY. The masses were selected based on the current SUSY model exclusion limits and to establish trends. The EWK W^+W^-jj phase space selection criteria from both ATLAS and CMS was first validated with SM VBS simulation and then applied to the SUSY simulations.

A modified profile likelihood ratio test was used to construct CL_s upper limits. The limits were calculated with pseudo-data toys because the asymptotic approximations were found to be invalid in the presence of large measurement uncertainties. Due to the established trends in the cross-sections, the upper limits were only calculated for the chargino mass points that produced the largest signals in the VBS phase space. One point had been previously excluded while the second had not.

The SUSY exclusion limits calculated in this channel were weaker than the current published exclusion limits. The SUSY exclusion limits could not be extended.

Based on the models tested, there is no significant impact to SM EWK W^+W^-jj measurements from Bino-Wino dichargino production at the current measurement precision level.

Future works could include investigating other types of VBS, such as same sign $W^{\pm}W^{\pm}$ or $W^{\pm}Z$, for SUSY contamination. Other BSM models that more closely suit the VBS signature could be utilized.

Bibliography

[1] M. E. Peskin and D. V. Schroeder, *An Introduction to quantum field theory*. Reading, USA: Addison-Wesley, 1995.

[2] C. P. Burgess and G. D. Moore, *The standard model: A primer*. Cambridge University Press, 12 2006.

[3] M. D. Schwartz, *Quantum Field Theory and the Standard Model*. Cambridge University Press, 3 2014.

[4] A. Rubbia, *Phenomenology of Particle Physics*. Cambridge, UK: Cambridge University Press, 6 2022.

[5] A. Buckley, C. White, and M. White, *Practical Collider Physics*. IOP, 12 2021.

[6] S. Navas *et al.*, "Review of particle physics," *Phys. Rev. D*, vol. 110, no. 3, p. 030001, 2024.

[7] M. E. Peskin, *Concepts of Elementary Particle Physics*. Oxford Master Series in Physics, Oxford University Press, 9 2019.

[8] A. Pich, "The Standard Model of Electroweak Interactions," in *2010 European School of High Energy Physics*, pp. 1–50, 1 2012.

[9] ATLAS Collaboration, "Observation of electroweak production of W^+W^- in association with jets in proton-proton collisions at $\sqrt{s} = 13$ TeV with the ATLAS detector," *JHEP*, vol. 07, p. 254, 2024.

[10] CMS Collaboration, "Observation of electroweak W+W− pair production in association with two jets in proton-proton collisions at s=13TeV," *Phys. Lett. B*, vol. 841, p. 137495, 2023.

[11] D. R. Green, P. Meade, and M.-A. Pleier, "Multiboson interactions at the LHC," *Rev. Mod. Phys.*, vol. 89, no. 3, p. 035008, 2017.

[12] P. Govoni, "Vector Boson Scattering: status and prospects," *PoS*, vol. CORFU2018, p. 007, 2019.

[13] ATLAS Collaboration, "Measurement and interpretation of same-sign W boson pair production in association with two jets in pp collisions at $\sqrt{s} = 13$ TeV with the ATLAS detector," *JHEP*, vol. 04, p. 026, 2024.

[14] CMS Collaboration, "Measurements of production cross sections of WZ and same-sign WW boson pairs in association with two jets in proton-proton collisions at $\sqrt{s} = 13$ TeV," *Phys. Lett. B*, vol. 809, p. 135710, 2020.

[15] ATLAS Collaboration, "Measurements of electroweak WZ boson pair production in association with two jets in pp collisions at $\sqrt{s} = 13$ TeV with the ATLAS detector," *JHEP*, vol. 06, p. 192, 2024.

[16] CMS Collaboration, "Evidence for WW/WZ vector boson scattering in the decay channel $\ell\nu$qq produced in association with two jets in proton-proton collisions at s=13 TeV," *Phys. Lett. B*, vol. 834, p. 137438, 2022.

[17] ATLAS Collaboration, "Fiducial and differential cross-section measurements of electroweak $W\gamma jj$ production in pp collisions at $\sqrt{s} = 13$ TeV with the ATLAS detector," *Eur. Phys. J. C*, vol. 84, no. 10, p. 1064, 2024.

[18] CMS Collaboration, "Observation of electroweak production of Wγ with two jets in proton-proton collisions at $\sqrt{s} = 13$ TeV," *Phys. Lett. B*, vol. 811, p. 135988, 2020.

[19] ATLAS Collaboration, "Measurement of the cross-sections of the electroweak and total production of a $Z\gamma$ pair in association with two jets in pp collisions at $\sqrt{s} = 13$ TeV with the ATLAS detector," *Phys. Lett. B*, vol. 846, p. 138222, 2023.

[20] CMS Collaboration, "Measurement of the electroweak production of Zγ and two jets in proton-proton collisions at $\sqrt{s} = 13$ TeV and constraints on anomalous quartic gauge couplings," *Phys. Rev. D*, vol. 104, p. 072001, 2021.

[21] ATLAS Collaboration, "Observation of electroweak production of two jets and a Z-boson pair," *Nature Phys.*, vol. 19, no. 2, pp. 237–253, 2023.

[22] CMS Collaboration, "Evidence for electroweak production of four charged leptons and two jets in proton-proton collisions at $\sqrt{s} = 13$ TeV," *Phys. Lett. B*, vol. 812, p. 135992, 2021.

[23] D. Buarque Franzosi *et al.*, "Vector boson scattering processes: Status and prospects," *Rev. Phys.*, vol. 8, p. 100071, 2022.

[24] D. L. Rainwater, R. Szalapski, and D. Zeppenfeld, "Probing color singlet exchange in Z + two jet events at the CERN LHC," *Phys. Rev. D*, vol. 54, pp. 6680–6689, 1996.

[25] ATLAS Collaboration, "Integrated and differential fiducial cross-section measurements for the vector boson fusion production of the Higgs boson in the $H \to WW^* \to e\nu\mu\nu$ decay channel at 13 TeV with the ATLAS detector," *Phys. Rev. D*, vol. 108, no. 7, p. 072003, 2023.

[26] Y. Nagashima, *Beyond the standard model of elementary particle physics*. Weinheim, USA: Wiley-VCH, 2014.

[27] G. Bertone and D. Hooper, "History of dark matter," *Rev. Mod. Phys.*, vol. 90, no. 4, p. 045002, 2018.

[28] C. Degrande, N. Greiner, W. Kilian, O. Mattelaer, H. Mebane, T. Stelzer, S. Willenbrock, and C. Zhang, "Effective Field Theory: A Modern Approach to Anomalous Couplings," *Annals Phys.*, vol. 335, pp. 21–32, 2013.

[29] C. P. Burgess, "Quantum gravity in everyday life: General relativity as an effective field theory," *Living Rev. Rel.*, vol. 7, pp. 5–56, 2004.

[30] J. F. Donoghue, "Introduction to the effective field theory description of gravity," in *Advanced School on Effective Theories*, 6 1995.

[31] B. Grzadkowski, M. Iskrzynski, M. Misiak, and J. Rosiek, "Dimension-Six Terms in the Standard Model Lagrangian," *JHEP*, vol. 10, p. 085, 2010.

[32] C. W. Murphy, "Dimension-8 operators in the Standard Model Effective Field Theory," *JHEP*, vol. 10, p. 174, 2020.

[33] J. J. Ethier, R. Gomez-Ambrosio, G. Magni, and J. Rojo, "SMEFT analysis of vector boson scattering and diboson data from the LHC Run II," *Eur. Phys. J. C*, vol. 81, no. 6, p. 560, 2021.

[34] S. P. Martin, "A Supersymmetry primer," *Adv. Ser. Direct. High Energy Phys.*, vol. 18, pp. 1–98, 1998.

[35] ATLAS Collaboration, "Search for direct production of charginos, neutralinos and sleptons in final states with two leptons and missing transverse momentum in pp collisions at $\sqrt{s} = 8$ TeV with the ATLAS detector," *JHEP*, vol. 05, p. 071, 2014.

[36] ATLAS Collaboration, "The quest to discover supersymmetry at the ATLAS experiment," *Phys. Rept.*, vol. 1116, pp. 261–300, 2025.

[37] ATLAS Collaboration, "Statistical Combination of ATLAS Run 2 Searches for Charginos and Neutralinos at the LHC," *Phys. Rev. Lett.*, vol. 133, no. 3, p. 031802, 2024.

[38] ATLAS Collaboration, "SUSY July 2024 Summary Plot Update," 2024.

[39] ATLAS Collaboration, "Searches for electroweak production of supersymmetric particles with compressed mass spectra in $\sqrt{s} = 13$ TeV pp collisions with the ATLAS detector," *Phys. Rev. D*, vol. 101, no. 5, p. 052005, 2020.

[40] ATLAS Collaboration, "Search for electroweak production of charginos and sleptons decaying into final states with two leptons and missing transverse momentum in $\sqrt{s} = 13$ TeV pp collisions using the ATLAS detector," *Eur. Phys. J. C*, vol. 80, no. 2, p. 123, 2020.

[41] ATLAS Collaboration, "Search for supersymmetry using vector boson fusion signatures and missing transverse momentum in pp collisions at $\sqrt{s} = 13$ TeV with the ATLAS detector," *JHEP*, vol. 12, p. 116, 2024.

[42] CMS Collaboration, "Combined search for electroweak production of winos, binos, higgsinos, and sleptons in proton-proton collisions at s=13 TeV," *Phys. Rev. D*, vol. 109, no. 11, p. 112001, 2024.

[43] B. C. Allanach, "SOFTSUSY: a program for calculating supersymmetric spectra," *Comput. Phys. Commun.*, vol. 143, pp. 305–331, 2002.

[44] ATLAS Collaboration, "A statistical combination of ATLAS Run 2 searches for charginos and neutralinos at the LHC." HEPData (collection), 2024. https://doi.org/10.17182/hepdata.149530.

[45] C. Bierlich *et al.*, "A comprehensive guide to the physics and usage of PYTHIA 8.3," *SciPost Phys. Codeb.*, vol. 2022, p. 8, 2022.

[46] J. Alwall, R. Frederix, S. Frixione, V. Hirschi, F. Maltoni, O. Mattelaer, H. S. Shao, T. Stelzer, P. Torrielli, and M. Zaro, "The automated computation of tree-level and next-to-leading order differential cross sections, and their matching to parton shower simulations," *JHEP*, vol. 07, p. 079, 2014.

[47] J. de Favereau, C. Delaere, P. Demin, A. Giammanco, V. Lemaître, A. Mertens, and M. Selvaggi, "DELPHES 3, A modular framework for fast simulation of a generic collider experiment," *JHEP*, vol. 02, p. 057, 2014.

[48] ATLAS Collaboration, "$E_{\mathrm{T}}^{\mathrm{miss}}$ performance in the ATLAS detector using 2015-2016 LHC *pp* collisions," 6 2018.

[49] CMS Collaboration, "Performance of missing transverse momentum reconstruction in proton-proton collisions at $\sqrt{s} = 13$ TeV using the CMS detector," *JINST*, vol. 14, no. 07, p. P07004, 2019.

[50] CMS Collaboration, "The CMS Experiment at the CERN LHC," *JINST*, vol. 3, p. S08004, 2008.

[51] ATLAS Collaboration, "The ATLAS Experiment at the CERN Large Hadron Collider," *JINST*, vol. 3, p. S08003, 2008.

[52] M. Dordevic, "The CMS Particle Flow Algorithm," *EPJ Web Conf.*, vol. 191, p. 02016, 2018.

[53] J. P. Mc Gowan, *Measurement of the electroweak production of a photon and a W boson in association with two jets in proton-proton collisions using the ATLAS Detector*. Phd thesis, McGill University, 2024.

[54] R. L. Workman *et al.*, "Review of Particle Physics," *PTEP*, vol. 2022, p. 083C01, 2022.

[55] A. Buckley, J. Ferrando, S. Lloyd, K. Nordström, B. Page, M. Rüfenacht, M. Schönherr, and G. Watt, "LHAPDF6: parton density access in the LHC precision era," *Eur. Phys. J. C*, vol. 75, p. 132, 2015.

[56] O. Behnke, K. Kröninger, T. Schörner-Sadenius, and G. Schott, eds., *Data analysis in high energy physics: A practical guide to statistical methods*. Weinheim, Germany: Wiley-VCH, 2013.

[57] J. Butterworth *et al.*, "PDF4LHC recommendations for LHC Run II," *J. Phys. G*, vol. 43, p. 023001, 2016.

[58] R. Brun and F. Rademakers, "ROOT: An object oriented data analysis framework," *Nucl. Instrum. Meth. A*, vol. 389, pp. 81–86, 1997.

[59] G. Cowan, K. Cranmer, E. Gross, and O. Vitells, "Asymptotic formulae for likelihood-based tests of new physics," *Eur. Phys. J. C*, vol. 71, p. 1554, 2011. [Erratum: Eur.Phys.J.C 73, 2501 (2013)].

[60] T. R. Junk, A. Korytov, and A. L. Read, *Statistical methods*. Hackensack: World Scientific, 2017.

[61] A. L. Read, "Modified frequentist analysis of search results (The CL(s) method)," in *Workshop on Confidence Limits*, pp. 81–101, 8 2000.

[62] T. Junk, "Confidence level computation for combining searches with small statistics," *Nucl. Instrum. Meth. A*, vol. 434, pp. 435–443, 1999.

[63] A. Nisati and V. Sharma, eds., *Discovery of the Higgs Boson*. Hackensack: World Scientific, 2017.